

## **General Disclaimer**

### **One or more of the Following Statements may affect this Document**

- This document has been reproduced from the best copy furnished by the organizational source. It is being released in the interest of making available as much information as possible.
- This document may contain data, which exceeds the sheet parameters. It was furnished in this condition by the organizational source and is the best copy available.
- This document may contain tone-on-tone or color graphs, charts and/or pictures, which have been reproduced in black and white.
- This document is paginated as submitted by the original source.
- Portions of this document are not fully legible due to the historical nature of some of the material. However, it is the best reproduction available from the original submission.

JPL PUBLICATION 84-17

(NASA-CR-173727) CLOUD COVER TYPING FROM  
ENVIRONMENTAL SATELLITE IMAGERY.  
DISCRIMINATING CLOUD STRUCTURE WITH FAST  
FOURIER TRANSFORMS (FFT) (Jet Propulsion  
Lab.) 65 p HC A04/MF A01

N84-28296

Unclas  
19831

CSCL 04B G3/47

# Cloud Cover Typing From Environmental Satellite Imagery

## Discriminating Cloud Structure With Fast Fourier Transforms

~ Thomas L. Logan  
James R. Huning  
David L. Glackin

January 31, 1983

Prepared for

U.S. Department of the Navy  
Naval Environmental Prediction  
Research Facility

Through an agreement with

National Aeronautics and Space Administration

by

Jet Propulsion Laboratory  
California Institute of Technology  
Pasadena, California

# **Cloud Cover Typing From Environmental Satellite Imagery**

## **Discriminating Cloud Structure With Fast Fourier Transforms**

Thomas L. Logan  
James R. Huning  
David L. Glackin

January 31, 1983

Prepared for  
U.S. Department of the Navy  
Naval Environmental Prediction  
Research Facility  
Through an agreement with  
National Aeronautics and Space Administration  
by  
Jet Propulsion Laboratory  
California Institute of Technology  
Pasadena, California

The research described in this publication was carried out by the Jet Propulsion Laboratory, California Institute of Technology, and was sponsored by the U.S. Department of the Navy through an agreement with the National Aeronautics and Space Administration.

Reference herein to any specific commercial product, process, or service by trade name, trademark, manufacturer, or otherwise, does not constitute or imply its endorsement by the United States Government or the Jet Propulsion Laboratory, California Institute of Technology.



## ABSTRACT

The Jet Propulsion Laboratory (JPL) has investigated the use of two-dimensional (2-D) Fast Fourier Transforms (FFTs) subjected to pattern recognition technology, for identification and classification of low altitude stratus cloud structure from Geostationary Operational Environmental Satellite (GOES) imagery. The research focus has centered on development of a preliminary scene independent pattern recognition methodology unconstrained by conventional cloud morphological classifications, with subsequent evaluation of the relationship between FFTs of satellite data and selected geophysical phenomena.

A methodology has been developed for extracting cloud shape, direction, and two size attributes from  $64^2$ ,  $32^2$ , and  $16^2$  pixel FFTs of GOES visual imagery. These four attributes were combined with two statistical attributes (cloud mean brightness, cloud standard deviation), and interrogated using unsupervised clustering and maximum likelihood classification techniques. Analysis of the results indicates that: 1) the key cloud discrimination attributes are mean brightness, direction, shape, and minimum size; 2) cloud structure can be differentiated at the  $16^2$  and  $32^2$  scales; 3) cloud type may be identifiable at coarser scales ( $64^2$  and above); 4) there are positive indications of scene independence which would permit development of a cloud signature bank; 5) edge enhancement of GOES imagery does not appreciably improve cloud classification over the use of raw data, and 6) the GOES imagery must be apodized before generation of FFTs. Substantiation of these results requires additional collateral rawinsonde and surface observations, and testing in different geographic areas over varying seasonal periods.

## ACKNOWLEDGEMENTS

The work reported herein was performed through NASA task order RD-182, Amendment 157, Proposal 80-1565 Revision A, by the Earth Resources Applications Group of the Image Processing Applications and Development Section (384), for the United States Navy, Naval Environmental Prediction Research Facility, in Monterey, California. Special appreciation is directed to the NEPRF contract monitors: Roland Nagle, Eve Schwartz, and David Lee, for their direction and support; as well as Jean J. Lorre for his assistance with the FFT science, and Elizabeth Davis for her excellent assistance in preparing the final report.

# TABLE OF CONTENTS

|  |     |
|--|-----|
| Abstract . . . . .   | iii |
| Acknowledgements . . . . .                                   | iv  |
| 1.0 INTRODUCTION . . . . .                                   | 1   |
| 1.1 Background Literature . . . . .                          | 1   |
| 1.2 Approach . . . . .                                       | 1   |
| 1.3 Scope . . . . .  | 1   |
| 2.0 DATA ACQUISITION, INTEGRATION, AND PREPROCESSING . . . . | 3   |
| 2.1 GOES Data and FFTs . . . . .                             | 3   |
| 2.2 Sea Surface Temperatures . . . . .                       | 4   |
| 3.0 FFT APODIZING . . . . .                                  | 9   |
| 3.1 Boundary Effects on FFTs . . . . .                       | 9   |
| 3.2 Apodizing the Data . . . . .                             | 9   |
| 3.3 Effects of Apodizing . . . . .                           | 10  |
| 4.0 FFT ATTRIBUTE GENERATION . . . . .                       | 14  |
| 4.1 Polar Coordinate Image . . . . .                         | 14  |
| 4.2 Cloud Direction Attribute . . . . .                      | 17  |
| 4.3 Cloud Size Attributes . . . . .                          | 18  |
| 4.4 Cloud Shape Attribute . . . . .                          | 20  |
| 4.5 Simulated FFT Analysis Test . . . . .                    | 22  |
| 4.6 Statistical Attributes . . . . .                         | 22  |
| 4.7 Orthogonality Test . . . . .                             | 24  |
| 5.0 CLASSIFICATION PROCEDURES . . . . .                      | 27  |
| 5.1 Unsupervised Clustering . . . . .                        | 27  |
| 5.2 Parallelepiped Maximum Likelihood Classification .       | 27  |
| 5.3 Dendrogram . . . . .                                     | 28  |
| 6.0 METEOROLOGICAL ELEMENTS . . . . .                        | 29  |
| 6.1 Collateral Meteorological Information . . . . .          | 29  |
| 6.2 Meteorological Setting . . . . .                         | 29  |
| 7.0 CLOUD CLASSIFICATION AND ANALYSIS . . . . .              | 34  |
| 7.1 32 x 32 Classification . . . . .                         | 34  |
| 7.2 Scene Independence . . . . .                             | 40  |
| 7.3 Scale Analysis . . . . .                                 | 41  |
| 8.0 EDGE ENHANCEMENT ANALYSIS . . . . .                      | 46  |
| 8.1 Image Convolution . . . . .                              | 46  |
| 8.2 Classification . . . . .                                 | 46  |
| 9.0 CONCLUSIONS AND RECOMMENDATIONS . . . . .                | 53  |
| 9.1 Conclusions . . . . .                                    | 53  |
| 9.2 Recommendations . . . . .                                | 53  |

|                           |    |
|---------------------------|----|
| 10.0 REFERENCES . . . . . | 55 |
|---------------------------|----|

## Figures

|       |   |    |
|-------|---|----|
| 1.    | GOES and SST data receipt from NEPRF . . . . .  | 5  |
| 2a-b. | Two-mile resolution GOES visual imagery of the<br>Southern California test area . . . . .   | 6  |
| 2c-d. | Two-mile resolution GOES visual and thermal<br>infrared imagery of the Southern California<br>test area . . . . .   | 7  |
| 3.    | Original Sea Surface Temperature data for Southern<br>California test area . . . . .  | 8  |
| 4.    | Diagrams showing the generation and removal of<br>spurious FFT spikes . . . . .   | 11 |
| 5.    | Unapodized FFTs of the 16 July imagery for 32x32<br>pixel areas . . . . .   | 12 |
| 6.    | Apodized FFTs of the 16 July imagery, showing<br>FFT's after removal of spurious spikes (Figure 5) .  | 13 |
| 7.    | Diagrams showing the steps involved in generating<br>a polar coordinate image from an unprocessed FFT .   | 15 |
| 8.    | Power spectra (average radial profiles) of five<br>FFT's. Arrows locate peaks representing average<br>cloud size . . . . .  | 16 |
| 9.    | To produce the cloud direction attribute, each<br>line (radial profile) in the polar coordinate<br>image is summed horizontally into a single column<br>to yield integrated FFT intensity as a function<br>of angle . . . . . | 16 |
| 10.   | The major axis of the clouds is the minor axis of<br>the FFT . . . . .  | 19 |
| 11.   | To produce the cloud size attribute, two average<br>radial profiles are derived from the polar coor-<br>dinate image, one along the axis of elongation<br>and one perpendicular to it . . . . .                               | 19 |

|     |  |    |
|-----|--|----|
| 12. | One measure of cloud shape that was investigated but not used in the final analysis has four quadrants in the polar coordinate image extracted and separately summed. They are then processed to yield a ratio . . . . . | 21 |
| 13. | Conceptualization of the process diagrammed in Figure 12 . . . . .   | 21 |
| 14. | A test of the CLOUDCLS algorithm to generate proper attribute information from simulated FFT images . . . . .  | 23 |
| 15. | Cloud attribute images produced from FFTs of three GOES visual images: (left to right) 6, 15, and 16 July 1981 . . . . .   | 25 |
| 16. | Pearson correlation matrix of the six cloud attributes . . . . .   | 26 |
| 17. | July mean Sea Surface Temperature in degrees Celsius . . . . .   | 30 |
| 18. | A generalized cross-section of cloud formation from off-shore to the coast . . . . .   | 30 |
| 19. | Rawinsonde data from San Nicolas Island and Pt. Mugu . . . . .   | 32 |
| 20. | Rawinsonde data of 17 July 1981 from Pt. Mugu . . .  | 33 |
| 21. | Stepwise cloud structure classification used to identify the best cloud attribute channels . . . .   | 36 |
| 22. | Raw four-attribute classification of 16 July data . . . . .  | 37 |
| 23. | Final 32x32-scale four-attribute cloud structure classification of 16 July 1981 GOES visual imagery . . . . .  | 38 |
| 24. | Final four-attribute cloud classification of 6 July imagery demonstrating the scene-independent properties of developed procedures . . . . .   | 39 |
| 25. | GOES imagery of 16 July with overlaid 16x16 pixel grid and the apodized FFTs produced from each box . . . . .  | 42 |

|     |   |    |
|-----|---|----|
| 26. | Final 16x16-scale four-attribute cloud structure<br>classification of 16 July GOES imagery showing<br>twenty-four classes grouped from the original<br>fifty formed . . . . . | 43 |
| 27. | Final 64x64-scale four-attribute cloud classifica-<br>tion of 16 July GOES imagery . . . . .  | 44 |
| 28. | Standard deviation convolution of 16 July and<br>6 July GOES visual imagery . . . . .   | 48 |
| 29. | Standard deviation convolutions of 16 July and<br>6 July thermal infrared imagery . . . . .   | 49 |
| 30. | FFT images of standard deviation convolved GOES<br>visual data . . . . .  | 50 |
| 31. | Cloud attribute images produced from FFTs of<br>three standard deviation (STD) convolved visual<br>GOES images . . . . .  | 51 |
| 32. | Final 32x32-scale four-attribute classification<br>of standard deviation-based attributes (Figure<br>31) of 16 July data . . . . .  | 52 |

## 1.0 INTRODUCTION

The Naval Environmental Prediction Research Facility (NEPRF) in Monterey, California, has a long range goal of developing a set of procedures for real time, large area identification and classification of atmospheric cloud types and structures. As one phase of this goal, the Jet Propulsion Laboratory (JPL) investigated the use of two-dimensional (2-D) Fast Fourier Transforms (FFTs) subjected to pattern recognition technology, for identification and classification of low altitude stratus cloud structure from Geostationary Operational Environmental Satellite (GOES) imagery. The primary research focus has centered on development of a preliminary scene-independent pattern recognition methodology unconstrained by conventional cloud morphological classifications, with subsequent evaluation of the relationship between FFTs of satellite data and selected geophysical phenomena.

### 1.1 Background Literature

The utility of Fast Fourier Transforms of meteorological satellite data for classification of atmospheric clouds has been demonstrated in a number of studies. Overviews of these studies can be found in a recent review by Toldalagi and Lebow (1982). The most recent cloud classification research employing FFTs was performed by Bunting and Fournier (1980). They calculated the average power spectra (radial profiles) of visual and infrared training sites representing nine conventional cloud categories and found a general separation between the power spectra of different cloud types. Comparison of power spectra with ground truth permitted classification of clouds.

### 1.2 Approach

This research utilized a different approach to FFT analysis than that used by Bunting and Fournier. The basic approach involved four steps, beginning with (1) the subdivision of each GOES visual and thermal infrared image into unique  $64 \times 64$ ,  $32 \times 32$ , and  $16 \times 16$  (i.e.,  $64^2$ ,  $32^2$ ,  $16^2$ ) pixel box regions and calculation of the 2-D FFT within each box. Software was developed (2) to extract the physical cloud attributes of size (two measures), shape, and direction from the 2-D FFTs. (Bunting and Fournier only investigated size using 1-D FFTs.) These derived data were combined with the mathematical attributes of mean brightness and standard deviation as calculated from the corresponding pixel regions, forming a data set of six channels in which each derived pixel represented the cloud attribute of the associated  $64^2$ ,  $32^2$ , or  $16^2$  pixel region. The six channel data set was (3) clustered using an unsupervised multispectral approach, and classified using a parallelepiped maximum likelihood procedure which incorporates a Bayesian decision rule (Addington, 1975). The resultant classification map was then (4) evaluated to determine relationships between the GOES data and cloud structure.

### 1.3 Scope

Pursuant to the primary goal of this research to develop a technical approach to cloud typing from FFTs, the scope was limited to identifying cloud structure in low and moderate altitude stratus. This reduced the distraction

that would have accompanied a more diverse data set. The Pacific Ocean study area off the California coast was chosen to include a time period when low altitude stratus dominated: 6 July through 31 July 1981. The study area included over one million square miles extending 1000 miles off the California coast. Cloud cover over land mass was not included in the analysis. GOES two-mile resolution visual (.55 to .70 micron) and thermal infrared (10.5 to 12.6 micron) imagery were supplied by NEPRF.



## 2.0 DATA ACQUISITION, INTEGRATION, AND PREPROCESSING

### 2.1 GOES Data and FFTs

Eighteen days of GOES visual (VS) and thermal infrared (IR) imagery were provided by NEPRF (Figure 1). The data represented one accession per day, corresponding to 1315 PDT for the VS data and 1345 PDT for the IR data. Both data sets were processed by NEPRF to represent equivalent two-mile 8-bit picture element (pixel) resolutions in a 512 by 512 pixel format. For each VS and IR image accession, NEPRF provided three sets of FFT data corresponding to 8 x 8, 16 x 16, and 32 x 32 pixel windows. These data were received in FFT 'complex' format, which consists of two single precision floating point values that represent the real and imaginary parts of the Fast Fourier Transform.

The eighteen days of VS and IR imagery were digitally contrast-enhanced as an aid in the selection of a smaller set of imagery for intensive interrogation. Three dates representing a wide variety of stratus cloud structure were chosen. These were 6, 15, and 16 July 1981 (Figure 2a-c).

The major utility of the thermal IR channel is its ability to differentiate cloud heights via temperature differences. Since only stratus clouds of relatively constant height were present in the selected data, the IR imagery provided a flat display of spectral information (Figure 2d), and were therefore dropped from subsequent analysis.

GOES image data from NEPRF were easily entered into JPL's VICAR (Video Image Communication And Retrieval) image processing software system (Castleman, 1979). VICAR contains over 300 modular software programs which can be sequentially linked to perform a wide variety of image processing applications. The software has been developed over the past fifteen years in support of the nation's unmanned space exploration program, including the recent Viking/Mars and Voyager/Jupiter/Saturn missions. However, the VICAR system does not reliably unblock data sets in which the record lengths are less than 360 bytes, so a logging (reformatting) program was written to perform this function (VNEPRF1). Later, a second program was written to move FFT origins (DC) from the corners to the center of the transform images (NFFTFLP).

To insure the complete compatibility of the NEPRF and JPL software technology, FFTs were generated at JPL from the raw GOES data using the following forward FFT computation:

$$\tilde{z}_{k\ell} = \sum_{m=0}^{M-1} \sum_{n=0}^{N-1} z_{mn} e^{-2\pi i \left[ \frac{km}{M} + \frac{\ell n}{N} \right]} \quad \text{for } k=0,1,\dots,M-1 \text{ and } \ell=0,1,\dots,N-1$$

where  $\tilde{z}_{k\ell}$  represents the output Fourier Transform value which is stored at pixel line  $\ell+1$ , pixel sample  $k+1$ ;  $z_{mn}$  represents the input data value at pixel

line  $m+1$ , pixel sample  $n+1$ ;  $M$  is the horizontal transform size,  $N$  is the vertical transform size, and both  $M$  and  $N$  are powers of two. (A generalization of the algorithm can be found in an article by Twogood and Ekstrom, 1976). After computation, the FFT is transposed along the diagonal. A perfect match between the NEPRF and JPL FFTs was obtained by scaling the NEPRF FFT by a factor of 10000.0 and scaling the JPL FFT by a factor of 9.7656.

For the visual display of the FFTs in this report, the following logarithmic transform enhancement was additionally applied:

$$(32767.0/\text{ALOG}(32767.0)) * \text{ALOG10}(\tilde{Z}_{kl})$$

Conversion to byte format for filmwriter display was accompanied by a linear contrast stretch of 6000 (becomes 0), 14000 (becomes 255), with all intermediate values 'stretched' in between.

## 2.2 Sea Surface Temperatures

Twelve days of Sea Surface Temperatures (SST) were obtained from Fleet Numerical Oceanography Center via NEPRF (Figure 1). The data were provided as collateral information to assist in comprehending cloud pattern and structure discernible in the GOES data, and to relate those patterns to subsequent classification results.

Sea Surface Temperature data (Figure 3a) were received as imagery in Polar Stereographic map projection measured at 12 GMT (4 PDT). The daily low sea-surface temperature varied from 6.0 degrees Celsius on 5 July 1981 to 1.7 degrees Celsius on 30 July. The highest temperature in the data set was 27.5 degrees Celsius and occurred over land. The highest sea-surface temperature was approximately 23 degrees Celsius.

In order to make use of the SST data, registration with the GOES data was necessary. To do this, the latitude/longitude coordinates provided by NEPRF for SST and GOES data were utilized. The SST coordinates were map-projected and therefore occurred in regular intervals. The unprojected GOES coordinates were not in the same regular intervals, so an intermediate coordinate grid was devised that both coordinate systems could be mapped to. This procedure provided the necessary common control points, and the registration was performed. In the situation where SST data were not available for the same days as the three selected GOES dates, SST data from the day before and after were averaged. The slow rate at which sea-surface temperature typically changes over a period of days precluded any significant error from being introduced by the averaging method. To assist in utilization of the SST registered data, a 'gradient direction' algorithm was applied to contour the data at two degree Celsius intervals. The filmwriter print (Figure 3b) shows cold (and missing data) areas as black, and hot areas as white.

| <u>July 1981 Date</u> | <u>SST<sup>1</sup></u> | <u>GOES<sup>2,3</sup></u> | <u>Notes</u>                 |
|-----------------------|------------------------|---------------------------|------------------------------|
| 5                     | *                      |                           |                              |
| 6                     |                        | *                         |                              |
| 7                     | *                      | *                         |                              |
| 8                     |                        | *                         |                              |
| 9                     | *                      | *                         |                              |
| 10                    |                        | *                         | GOES VS and IR Data Dropouts |
| 11                    |                        |                           |                              |
| 12                    | *                      |                           |                              |
| 13                    |                        | *                         |                              |
| 14                    | *                      | *                         |                              |
| 15                    |                        | *                         |                              |
| 16                    | *                      | *                         |                              |
| 17                    |                        | *                         | GOES VS duplicate of 16 July |
| 18                    |                        |                           |                              |
| 19                    | *                      |                           |                              |
| 20                    |                        | *                         |                              |
| 21                    | *                      | *                         |                              |
| 22                    |                        | *                         |                              |
| 23                    | *                      | *                         |                              |
| 24                    |                        |                           |                              |
| 25                    |                        |                           |                              |
| 26                    | *                      |                           |                              |
| 27                    |                        | *                         |                              |
| 28                    | *                      | *                         |                              |
| 29                    |                        | *                         | 23 lines of GOES IR garbled  |
| 30                    | *                      |                           |                              |
| 31                    |                        | *                         |                              |


---

1 12GMT

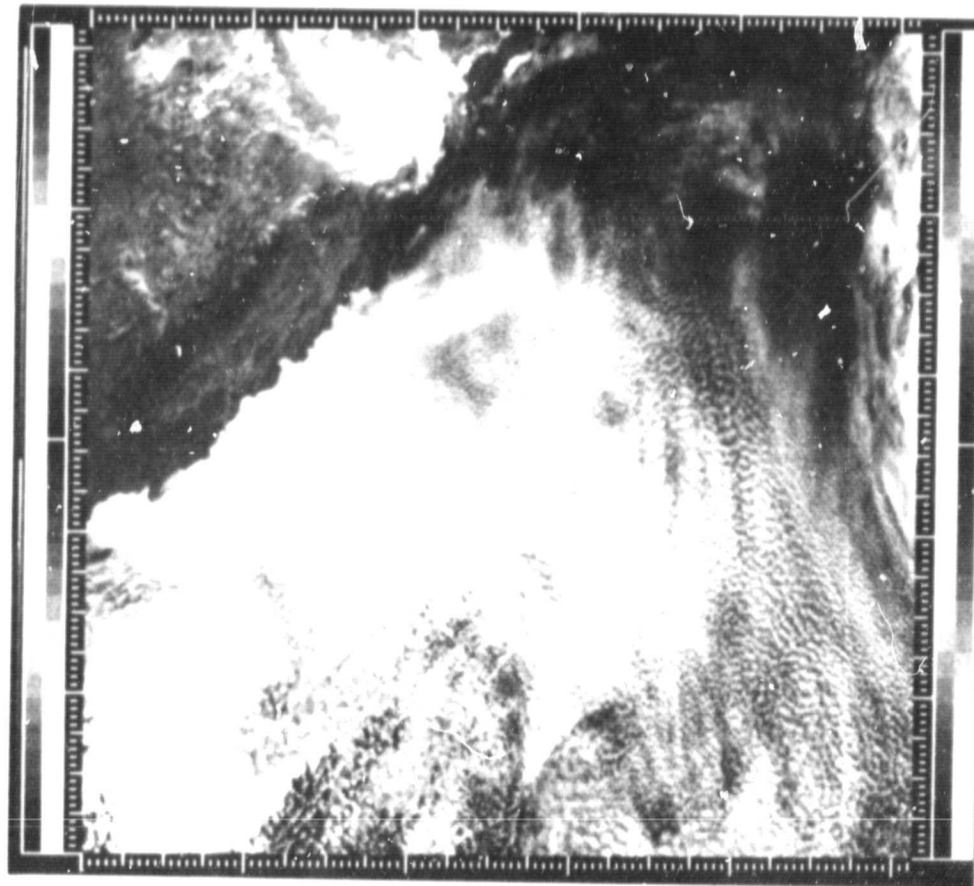
2 VS 1315PDT

3 IR 1345PDT

Figure 1. GOES and SST data receipt from NEPRF

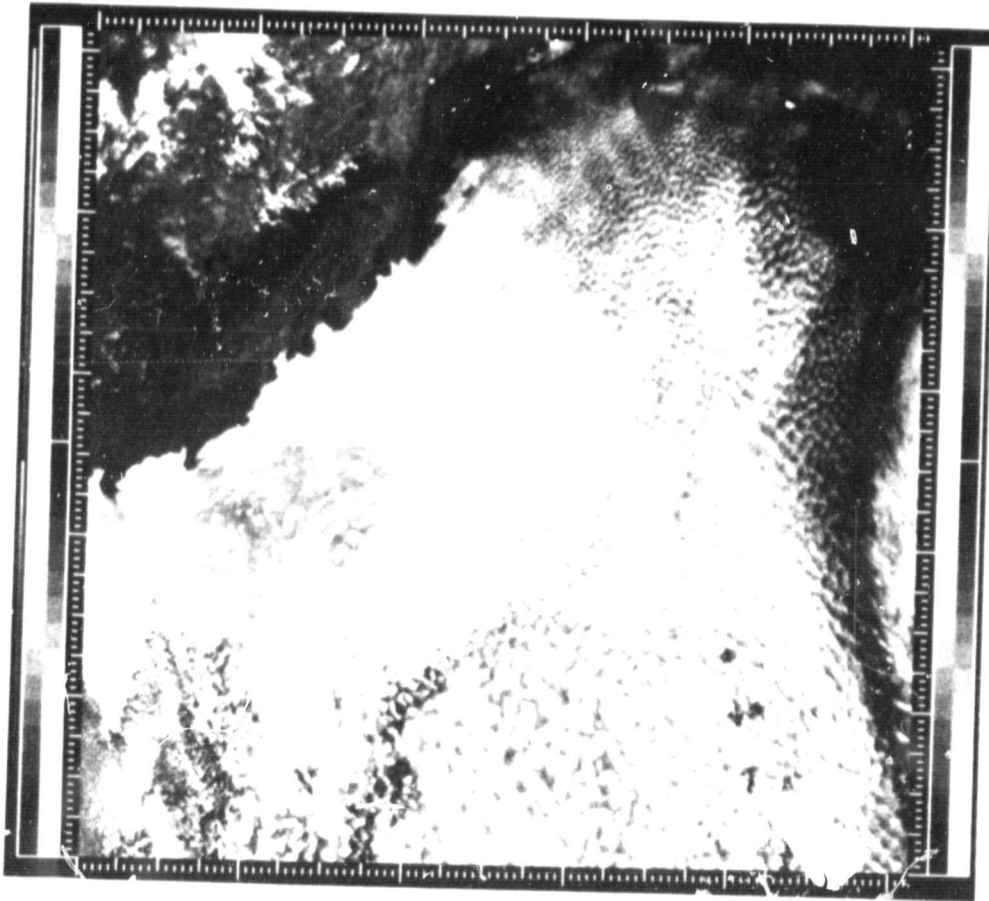


(a)

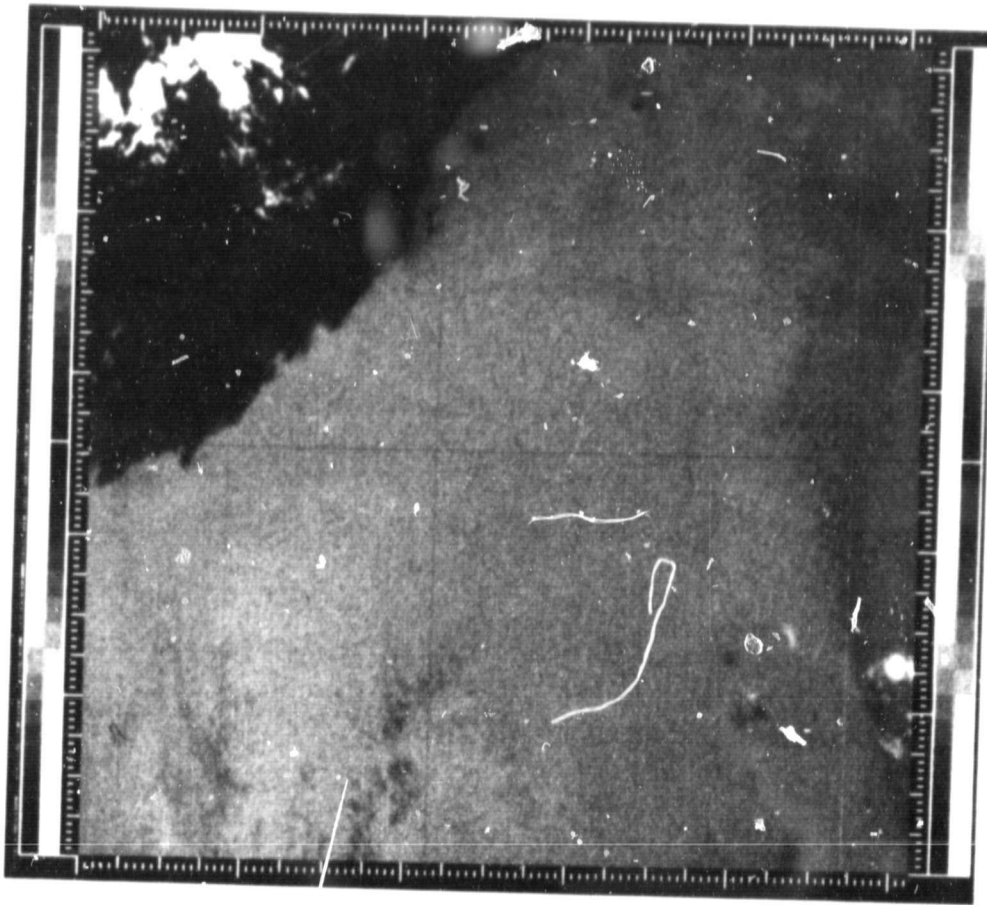


(b)

Figure 2a-b. Two-mile resolution GOES visual imagery of the Southern California test area. Left (a), imagery for 6 July, 1981; Right (b), imagery for 15 July, 1981.

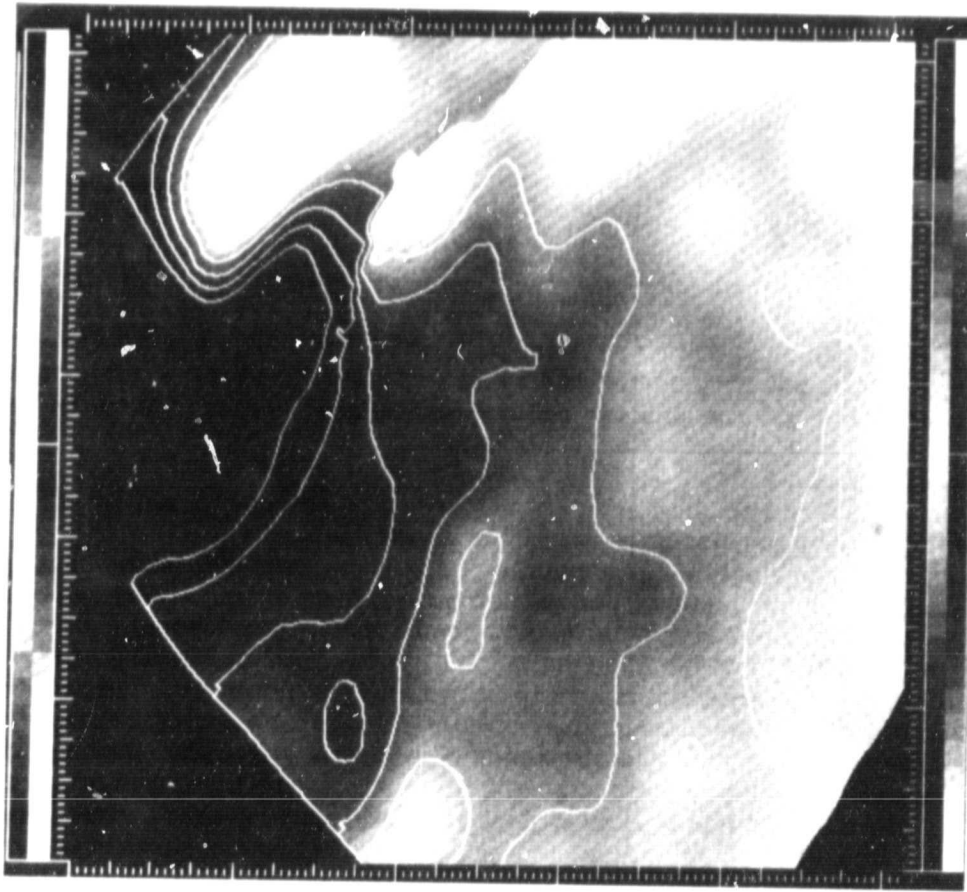


(d)

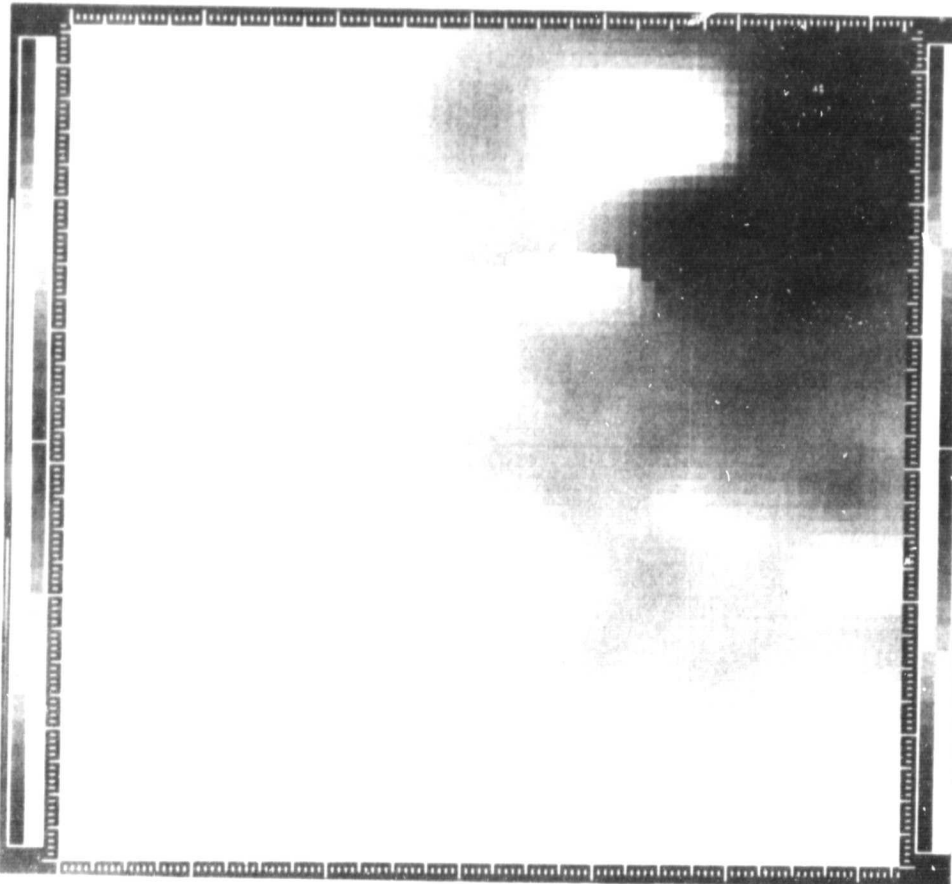


(c)

Figure 2c-d. Two-mile resolution GOES visual (left, d) and thermal infrared (right, c) imagery of the Southern California test area for 16 July, 1981.



(b)



(a)

Figure 3. Original Sea Surface Temperature data for Southern California test area provided by NEPRF (a), and after contouring and registration to 16 July GOES imagery (b). Temperatures are in degrees Celsius.

### 3.0 FFT APODIZING

Fast Fourier Transforms of areas with highly contrasting brightness values can experience undesirable bright spikes along the x and y axes of the transform. These artifacts occur when a large pixel digital number (DN) difference exists between the beginning and end points of the data subjected to FFT transformation. The spikes obscure real FFT signal information by confusing the subsequent FFT analysis algorithms. Apodizing the raw data before transformation can reduce or eliminate the spike problem.

#### 3.1 Boundary Effects on FFTs

Bright spike artifacts in FFTs are caused by pixel brightness boundaries such as those occurring at the land/water and cloud/no cloud interfaces. For example, consider an idealized box containing a cloud/no cloud boundary (Figure 4a). An illustration of the one-dimensional FFT problem can be made using a single line through the box. The profile of the brightness values taken horizontally across the box would start with a high DN value and decrease to a low DN value (Figure 4b). Because the Fourier Transform requires an infinite string of data to work on (Figure 4c), it repeats the same line of data infinitely. The sudden vertical jump that occurs in the signal at the beginning of the 'repeat' results in spurious data. In the two-dimensional FFT, the jump occurs because the beginning and end points in either horizontal or vertical directions are not the same. The resulting spurious signal in the transform appears as bright spikes along the x and/or y axes of the transform (Figure 4d).

The bright spike artifacts can be clearly seen in the first images produced of the FFTs (Figure 5). They are most obvious in regions where there are holes in the clouds or sudden changes or breaks in the cloud pattern, particularly along the cloud/land interface in the upper right portion of Figure 5. Any grid boxes in which the DN's are significantly different along opposite edges of the box will have spike problems.

The dilemma posed by the bright spikes is that very similar signals can also be produced by real clouds. For example, a pattern of long and skinny vertical clouds would have a strong FFT signal along the horizontal axis. This is important information that would appear to be very similar to the spurious data. Differentiation of the spurious data from the real data must be made or cloud typing results will be in error; the software that generates the cloud attributes (Section 4) tends to 'lock on' to the spikes. If the spike represents spurious data, then the program will output spurious cloud attributes.

#### 3.2 Apodizing the Data

The usual solution for treating the spike problem in FFTs is to 'apodize' or 'mask' the raw data before transformation. Apodizing is the process of smoothing the border of each box such that large DN differences are reduced to a smooth transition. The process must be applied to the raw data, however, and after apodizing, the original values are lost (i.e., replaced by the

smoothed values). Apodizing is performed by applying a cosine function to those pixels at the edges of each box such that the pixel DN's smoothly ramp up or down to some average DN level (Figure 4e). The resulting lack of sharp discontinuities in the data eliminates most or all of the spurious signal in the transformation (Figure 6). Since a minimum of three points is needed to define a curve, the masked region must be at least three pixels wide. This means that for 8 x 8 boxes, there would only be a central square of four pixels of usable data left. Hence, they cannot be apodized. Since lack of apodizing would permit serious artifacts to appear in the FFTs, 8 x 8 FFTs cannot be investigated.

An alternative to conventional apodizing was also tested. The alternative method assumed that the width of the spurious signal along the axis would be exactly one pixel wide. Presumably, the width of the signal from real clouds would be several pixels, because clouds tend to be fuzzy and are rarely perfectly straight and parallel. Thus, simple interpolation using the pixel values in the transform before and after the pixel on the axis would theoretically remove the spurious signal and leave the real signal. After testing and analysis, however, it was determined that the spurious signals were often two to three pixels and occasionally five pixels wide for the 32 x 32 grid case. This alternative method was therefore discarded.

### 3.3 Effects of Apodizing

Edge pixels that are modified by the apodizing process represent lost information. This loss is beneficial when the result is the removal of bright spikes that obscure real information, but it is undesirable when apodizing is applied to a grid cell not requiring it. In this research, all cells were apodized because a reliable measure of an FFT's need for apodizing was not available, and because selective apodizing would have reduced the comparability of the FFTs.

Several qualitative and quantitative tests were performed to determine the effect of apodizing grid cells not requiring the operation. Qualitative inspection of apodized and unapodized transforms indicated that minor changes did occur in FFT shape and direction. Pixel listings and histograms of selected apodized and unapodized transforms indicated a decrease in statistical mean by six DN.

A more definitive test was made by generating cloud attribute data (section 4) from apodized and unapodized FFTs, followed by classification (section 5). Comparison of the cloud attribute data showed differences in cloud shape, direction, maximum size, and minimum size. However, these differences are not necessarily undesirable, as the classification results indicated that apodizing considerably improved discriminability from all FFTs, including those which did not have a noticeable spike problem. Apparently, subtle errors are produced when beginning and end points of a grid cell are not apodized, even in cases where the jump in DN is not large. This indicates that the raw data should always be apodized.



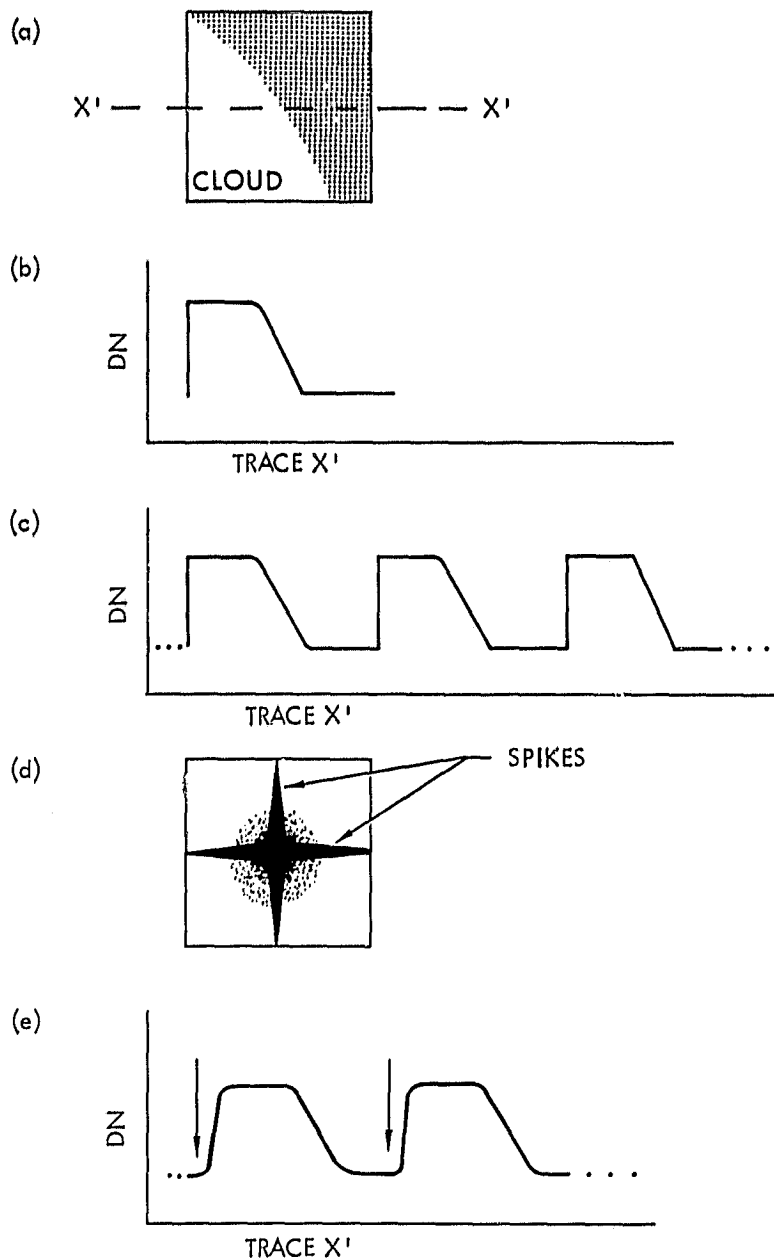


Figure 4. Diagrams showing the generation and removal of spurious FFT spikes. A densitometer (brightness) profile (b) of a trace (a), taken across image data containing a cloud/no-cloud boundary, shows a major DN change between the beginning and end points of the profile. FFT mathematics require an infinite repetition of the profile (c), and the resulting sudden brightness step is interpreted as information, which results in bright spikes in the FFT (d). Apodizing the image data prior to FFT generation results in a smoothing of the profile's beginning and end points (arrow, e), which suppresses the spikes.

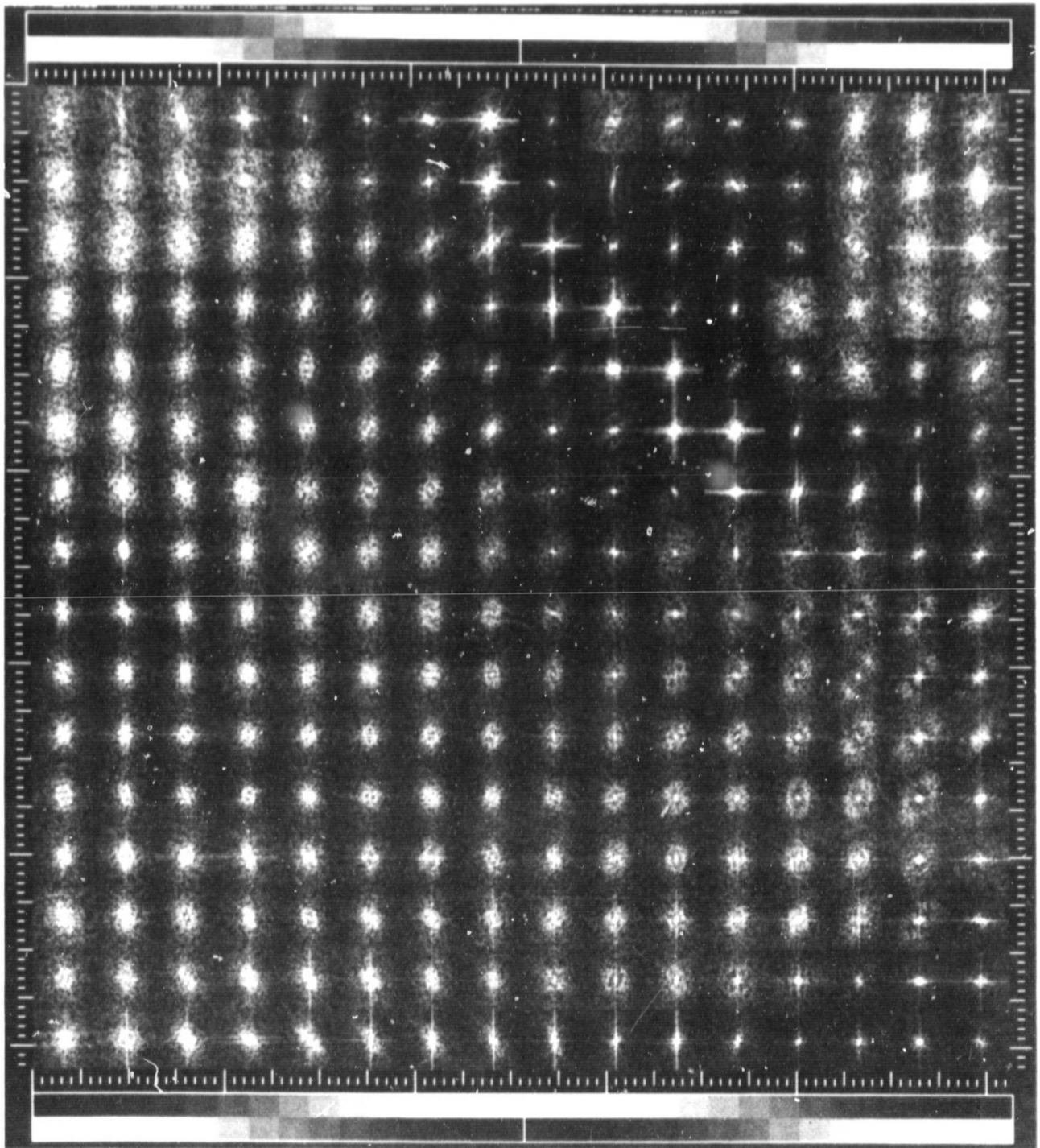


Figure 5. Unapodized FFTs of the 16 July imagery for 32x32 pixel areas. Spurious information caused by discontinuities in the image data show as spikes.

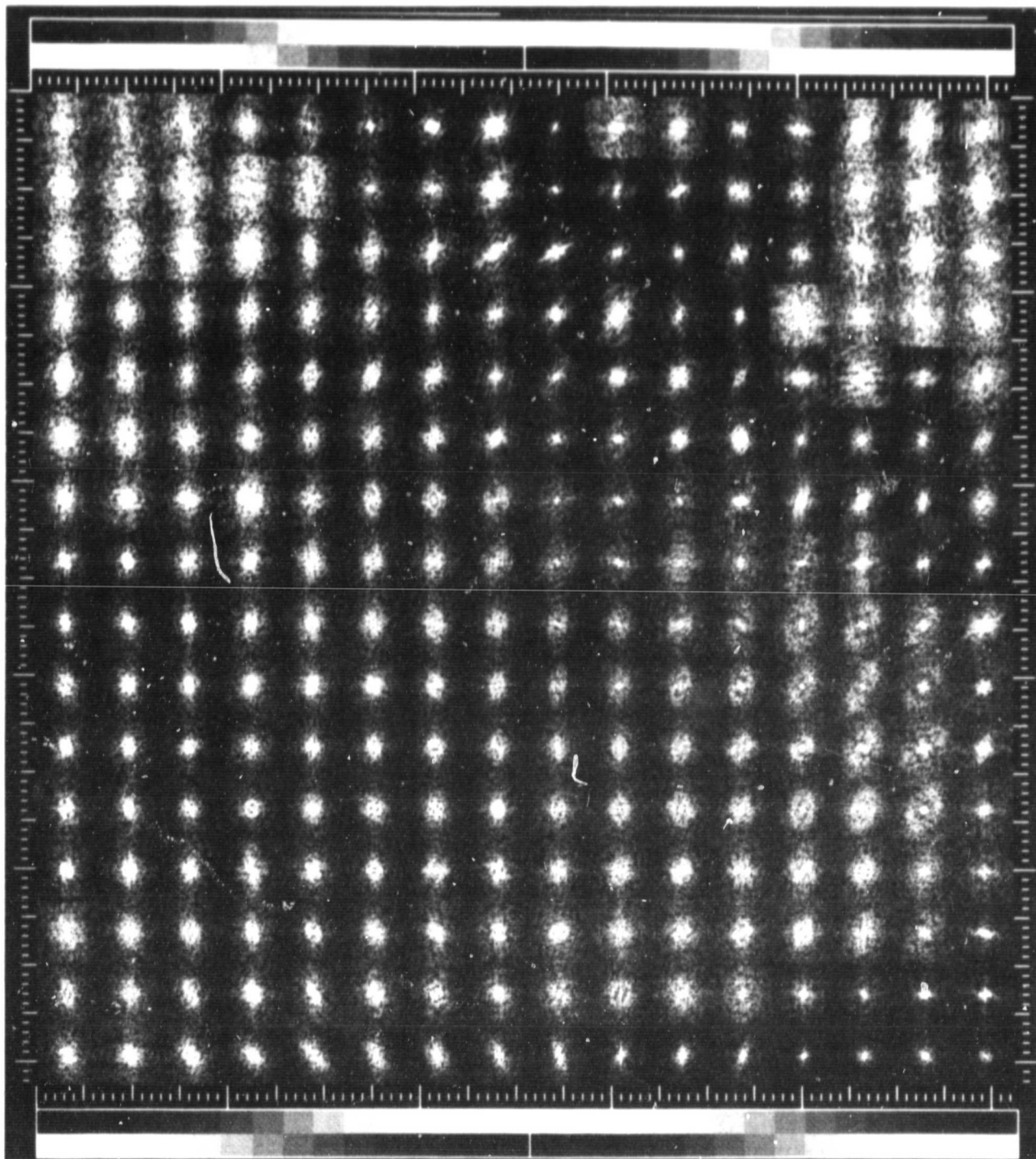


Figure 6. Apodized FFTs of the 16 July imagery, showing FFTs after removal of spurious spikes (Figure 5). Each FFT is an expression of a 32x32 pixel box of the GOES imagery (Figure 2c).

## 4.0 FFT ATTRIBUTE GENERATION

An FFT in image format can be digitally interrogated to extract attribute (parameter) information describing the original data. Four attributes of the FFT were selected as the most relevant descriptors of cloud structure. These are direction, shape, and two measures of size, and are referred to as 'physical' attributes because they represent indirect measurements of cloud pattern and structure via the FFT. Two additional attributes, mean brightness and standard deviation, were generated and are referred to as 'statistical' attributes because of their simple statistical derivation. Both physical and statistical attributes were derived for the non-overlapping consecutive  $64^2$ ,  $32^2$ , and  $16^2$  boxes, resulting in six separate images.

It is important to note that the physical attributes are a representation of the entire set of interacting properties occurring within the box over which the FFT is taken. The precise way in which this convolution occurs is not immediately obvious, since it occurs in complex space and involves FFT phase as well as amplitude. The size and shape of the two-dimensional FFT are closely coupled to the physical size and shape of the clouds, since cloud size and pattern size, and cloud shape and pattern shape are empirically coupled in reality. A new software program called CLOUDCLS was written to extract the physical cloud attributes from the FFT.

### 4.1 Polar Coordinate Image

Before calculation of the direction, shape, and size attributes, the image of the Fast Fourier Transform is converted into a polar coordinate image by the CLOUDCLS program. Three steps are necessary to produce a suitable polar coordinate image.

An FFT is composed of four quadrants, of which two are mirror images. The FFTs from NEPRF had the origin (DC) located in the upper left corner (Figure 7a), so the quadrants were (1) rearranged as shown in Figure 7b. The origin (DC) is placed in the center of the box (offset one pixel) with the first entire row and column of data ignored (Nyquist frequency). This produces a symmetric FFT which is necessary for subsequent calculations. A  $32 \times 32$  pixel transform, for example, essentially contains only  $31 \times 31$  pixels of data with the DC located at the center. To produce the polar coordinate image, (2) concentric circles of data centered around DC are 'uncurled' (Figure 7c) to form a column of equal length in the output image. Corners of the  $31 \times 31$  box are not used so as to equally weight all directions and prevent bias in the calculation of FFT shape. Obviously there is a great deal of interpolation involved, with the first 'uncurled' column essentially representing the repeated sequence of a single value (DC), and the last circular extraction (at the maximum radius, i.e., box edge) containing the largest quantity of unique information (Figure 7d). The polar coordinate image of an FFT can only have a maximum number of columns and rows equal to the number of pixels in its radius (e.g., 16 for a  $32^2$  FFT).

The average radial profile (power spectrum) represents all column data in the polar coordinate image averaged into a single line (Figure 7e). Figure 8

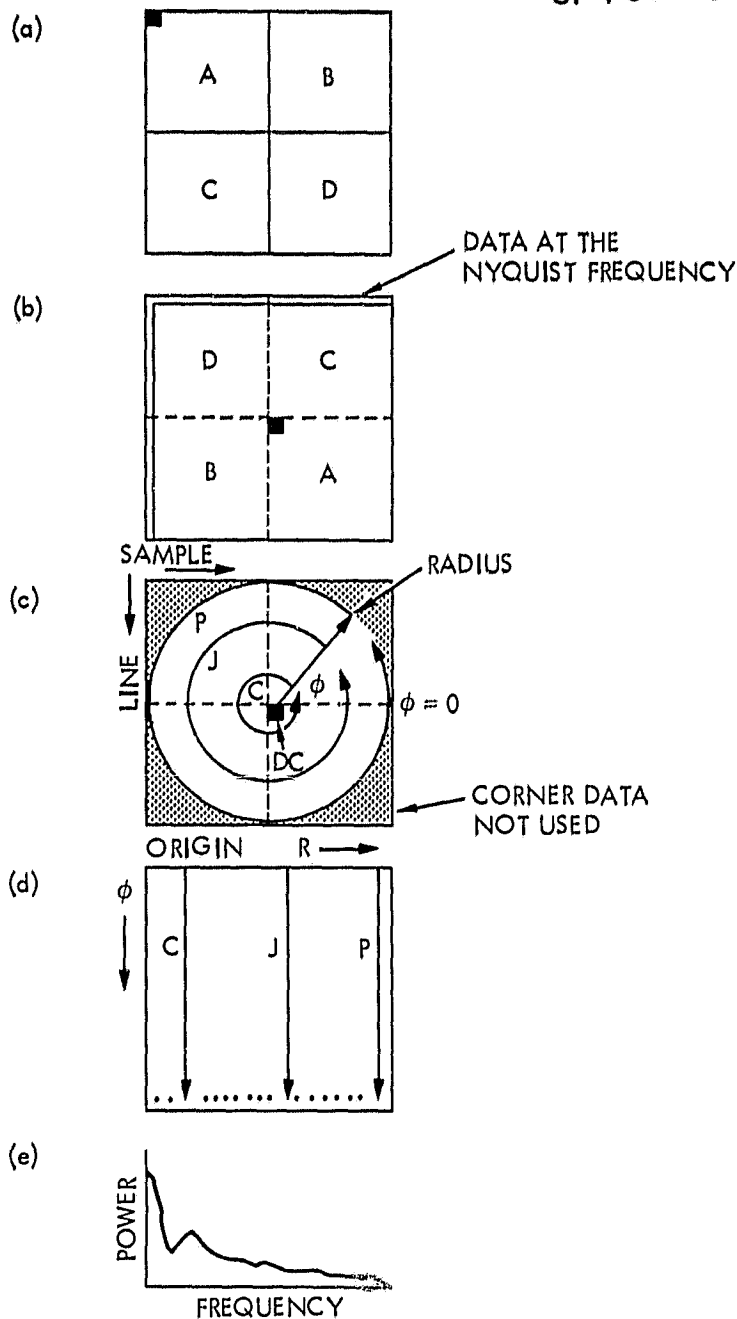


Figure 7. Diagrams showing the steps involved in generating a polar coordinate image (d) from an unprocessed FFT (a). FFTs from NEPRF (a) were rearranged to place the origin near the center of the box (b). The first row and column of FFT data are spurious (Nyquist Frequency) data and are ignored (b). The polar coordinate image is produced by taking circles of data (C,...,J,...P) that begin and end at the same point on a radius from DC to the box edge and uncurling them to form a column of equal length in the output image (d). Bilinear interpolation is used to give all uncurred data the same length (d). The average radial profile (power spectrum) is an average of the rows in the polar coordinate image (e).

ORIGINAL PAGE IS  
OF POOR QUALITY

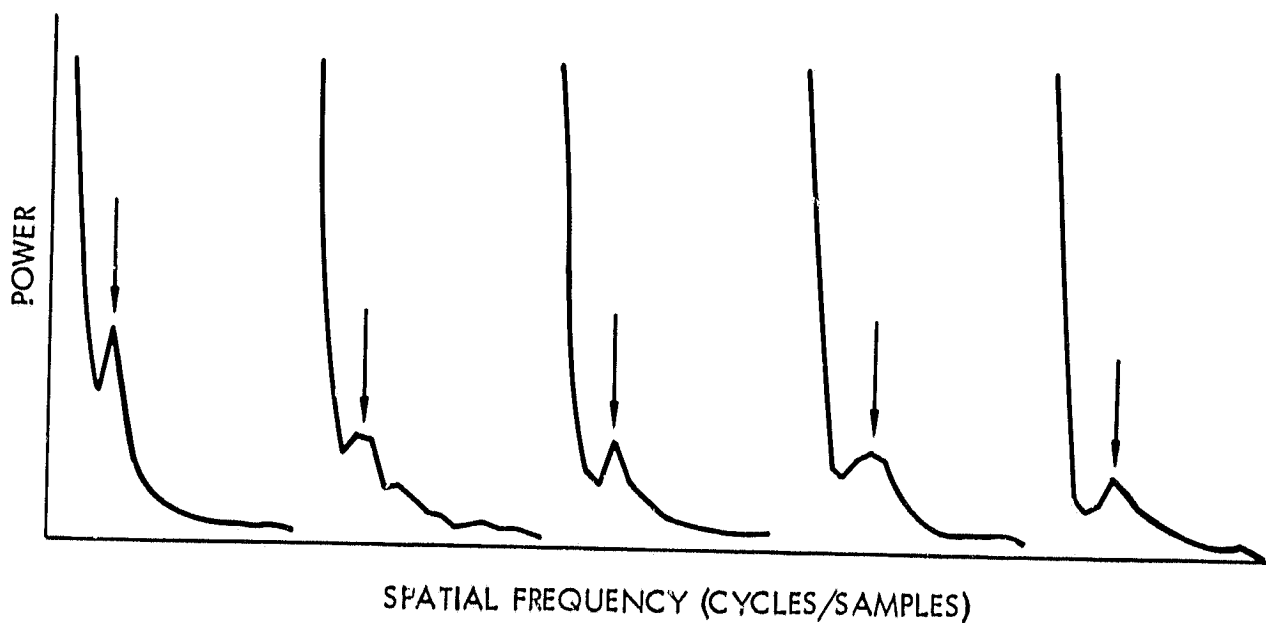


Figure 8. Power spectra (average radial profiles) of five FFTs. Arrows locate peaks representing average cloud size.

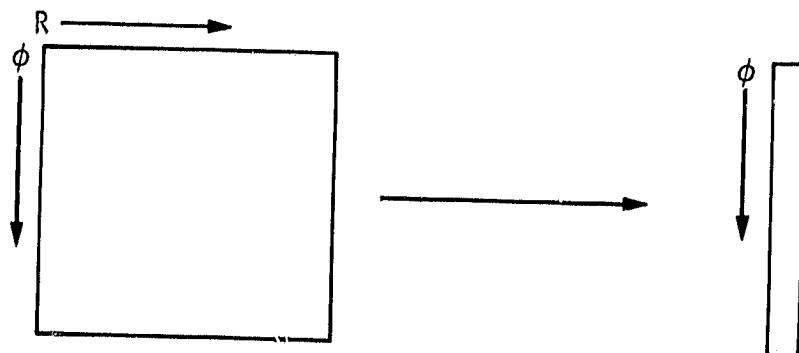


Figure 9. To produce the cloud direction attribute, each line (radial profile) in the polar coordinate image is summed horizontally into a single column to yield integrated FFT intensity as a function of angle.

contains the average radial profiles of several actual individual FFTs and reveals a peak that is indicative of the average cloud size (section 4.3).

Finally, (3) a logarithmic scaling was performed to prevent the very highest power data from overwhelming the majority of data in the polar coordinate image:

$$((32767.0/\text{ALOG}(32767.0)) * (255/14230)) * \text{ALOG10}(\text{DN})$$

where: 14230 represents the highest FFT pixel brightness value (excluding DC), and DN represents the input FFT pixel digital number.

#### 4.2 Cloud Direction Attribute

The cloud direction attribute measures the angle of the cloud's major axis counterclockwise from north. It does not denote the direction of cloud movement. The attribute keys on the major axis of cloud elongation in the box and is therefore responsive to the interplay of cloud size/pattern and box size. The 16 x 16 box would probably yield a more accurate measurement than a larger box because there would be less chance for pattern variation to occur. However, if the cloud pattern is consistent, very reliable measures can be obtained. Visual accuracy checks indicate that the computed angle is usually within 10 degrees of the expected value. Round cloud patterns are flagged as 'indeterminant' (i.e., saturated to a DN value of 255).

To produce the cloud direction attribute, each line (radial profile) in the polar coordinate image is summed into one value (Figure 9). This results in a single column of pixels representing the FFT's integrated intensity as a function of angle. Since the transform of an elongated cloud pattern is generally elliptical, the column will contain two maxima and two minima. The orientation angle is found by taking the one-dimensional Fourier Transform of the column and extracting the phase of the third term (which represents the two maxima and minima in the column). The FFT will be elongated in a direction perpendicular to that in which the clouds are elongated; therefore, a 90-degree adjustment is made to restore the attribute as a measure of cloud direction rather than FFT direction. The actual computations are:

$$(1) \quad R + iI = \sum_{n=0}^{m-1} b_n e^{-2\pi i 2n/m}$$

$$(2) \quad \text{angle } \phi = \tan^{-1} \frac{I}{R}$$

$$(3) \quad \text{north angle} = \frac{(2\pi - \phi) 180}{2\pi} + 90$$

where: R = the real component of the 1-D FFT;  
 I = the imaginary component of the 1-D FFT;  
 m = the number of pixels; and  
 b = the integrated intensity of the 2-D FFT as a function of angle (i.e., the horizontally summed radial profiles).

### 4.3 Cloud Size Attributes

Two measures of cloud size were produced corresponding to the major axis (S maj) and minor axis (S min) of the cloud. The cloud's major axis is the minor axis of the FFT (Figure 10).

FFT size relates closely to cloud size. The size computation is considered to be quite good and reliable although the major axis calculation is slightly less consistent and repeatable than the minor axis calculation. In 14% of the (16 July) 32 x 32 FFT cells, S min was calculated to be greater than S maj. Most of these situations can be attributed to oddities in cloud data (odd shape; land contamination). Only 2% of the errors were unexplained. This error is considered to be well within prudent limits.

Four techniques were investigated for calculating cloud size from the average radial profile (power spectrum). The first method utilized the well known characteristic of the power spectrum for showing scale sizes (or periodicities) in data. Usually a peak (excluding DC) in the profile indicates the characteristic size (Figure 8). Many of the cloud FFTs, however, simply possess a bright spike at their DC component and then smoothly decrease in intensity with increasing radius. Thus, a peak-searching algorithm would not be generally applicable.

The second method used a simple minimum/maximum ratio of two areas in the average radial profile. A dividing line was chosen such that for the largest clouds, very little power would occur to the right of it. The ratio would be empirically calibrated to reveal different sizes and the threshold of 'indeterminacy.'

A third method paralleled the second except that two average radial profiles were computed. These profiles were derived from the areas in the polar coordinate image that contained information along the axis of elongation and perpendicular to the axis of elongation (Figure 11).

Empirical tests of these two methods revealed neither to sufficiently discriminate size. A fourth approach was therefore derived which employed the normalized second moment of the radial profile.

The second moment is obtained by multiplying the power (y-axis) of each point in the radial profile by the square of the distance of that point along the x-axis. Both the DC pixel and a few pixels at the edge (maximum radius in the polar coordinate image) are omitted (the latter represent noise). The normalization is performed through a division by the sum of powers of the area under the radial profile curve. By using this normalization, a brighter layer of clouds and a fainter layer of clouds of the same size will both yield the same size attribute. The equation is:

$$\text{size attribute} = \frac{1}{\sum \text{power}} \sum_{x=2,n} \text{power} \quad x^2$$



ORIGINAL PAGE IS  
OF POOR QUALITY

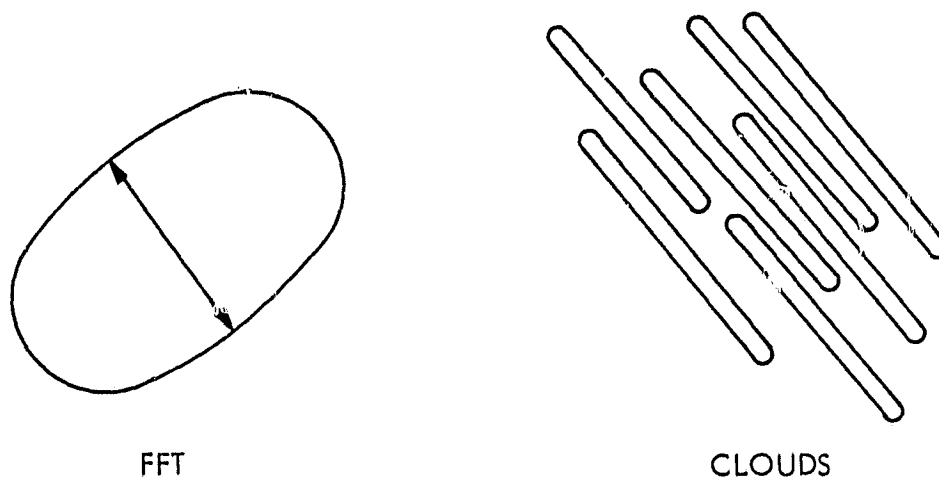


Figure 10. The major axis of the clouds is the minor axis of the FFT.

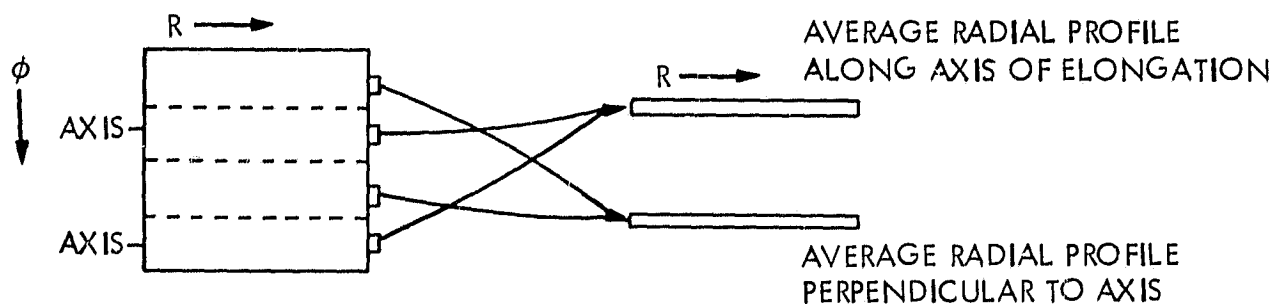


Figure 11. To produce the cloud size attribute, two average radial profiles are derived from the polar coordinate image, one along the axis of elongation (major axis) and one perpendicular to it (minor axis).

where  $x$  is the numeric index value of the power along the  $x$ -axis. For  $32 \times 32$  FFTs which have radial profiles of length 16, pixel values above  $n=12$  were excluded as noise. For  $16 \times 16$  FFTs, the profile length is 8, and pixel values above  $n=6$  were excluded. For  $64 \times 64$  FFTs,  $n = 24$  was used.

In the case of small clouds, the values above  $n=12$  (for  $32^2$  FFTs) actually contain some useful information. An attempt was made to evaluate the improvement in small cloud discriminability versus large cloud degradation by extending the range of  $n$ . Results indicated that overall discriminability was reduced, and that the above cutoffs were optimal.

The normalized second moment technique produces an acceptable measurement of maximum and minimum cloud size. To insure that the resultant numbers were in the same histogram range as those produced for the direction and shape attributes, a post-stretch was applied. This prevented the size parameters from being statistically underweighted relative to the others in the subsequent multivariate classification step.

The final tested approach used the normalized third moment of the radial profile. It was thought that this weighting would help to enhance small clouds without unduly magnifying the noise component. Empirical testing did not substantiate the hypothesis, however, and discrimination was less than when utilizing the second moment.

#### 4.4 Cloud Shape Attribute

The cloud shape attribute is the most sensitive to unevenness in cloud pattern, but performs satisfactorily as long as the patterns are not excessively variable. Shape discriminability could theoretically be improved by using a smaller box size.

Four methods of measuring shape were investigated. The first used the polar coordinate image and the axis of elongation obtained from the direction calculation. The procedure divides the polar coordinate image into four quadrants (each 90 degrees wide), and places two quadrants symmetrically about the axis of elongation. The quadrants are then summed to produce a minimum/maximum ratio (Figure 12). The ratio will vary between 0 and 1, with the more elongated clouds corresponding to the lower ratios. The process is conceptualized relative to the original FFT in Figure 13. The method was found to be only moderately discriminatory of shape because of its inherent blending of information across entire FFT quadrants.

A second measure of cloud shape utilized the eccentricity of an ellipse fitted to the shape of the FFT. The resulting attributes closely matched those produced by the first method.

The third method used the ratios of the unnormalized second moments produced in the cloud size computation. As a part of the evaluation, the normalized second moments were also tested, but they proved less discriminatory. Use of the unnormalized second moments for calculation of the shape attribute proved superior to the first two methods. The optimal selected limits were  $n = 3$  to 14 for  $32 \times 32$  FFTs, and  $n = 6$  to 28 for  $64 \times 64$  FFTs.

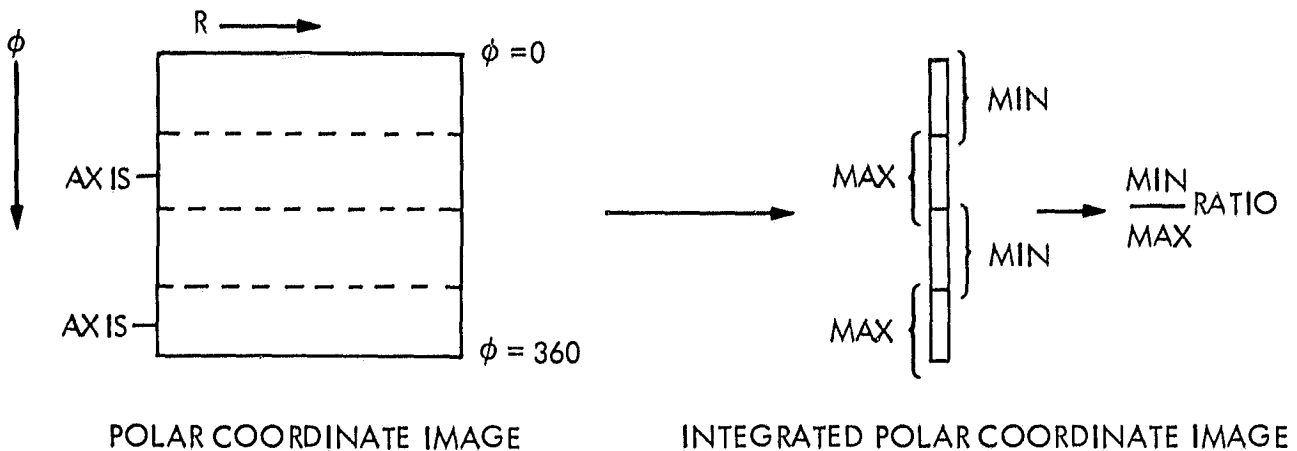


Figure 12. One measure of cloud shape that was investigated but not used in the final analysis has four quadrants in the polar coordinate image extracted and separately summed. They are then processed to yield a ratio. The actual method used to generate the cloud shape attributes is described in the text.

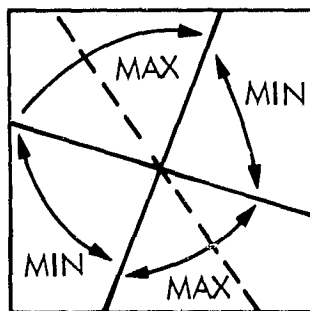


Figure 13. Conceptualization of the process diagrammed in Figure 12. The division into quadrants is shown here for the FFT in its original form, where the diagonal dashed line is the axis of elongation (major axis).

The fourth method used the ratios of the unnormalized third order moments, with the same rationale as for the size attribute. But like the size computation, extensive analysis revealed this method to be significantly less discriminatory of shape than the unnormalized second moment.

A goal of attribute computation is that they be linear. This is difficult with size and shape because the second moment is not precisely related to cloud size and shape in a linear manner. However, the general curve of a radial profile is that of a second order polynomial, so the second moment is the closest to being linear relative to cloud size and shape of any mathematical moment. Although the second moment technique does allow some discriminatory overlap to occur in shape calculation, it is not serious, and the method is superior to the other techniques.

#### 4.5 Simulated FFT Analysis Test

As a means for evaluating the overall accuracy of FFT attribute computation, ten simulated FFTs were generated in the form of solid circles and ellipses of various sizes, shapes, and orientations. While the test objects do not fully emulate true FFTs, the patterns are sufficient to verify the operation of the CLOUDCLS attribute software program.

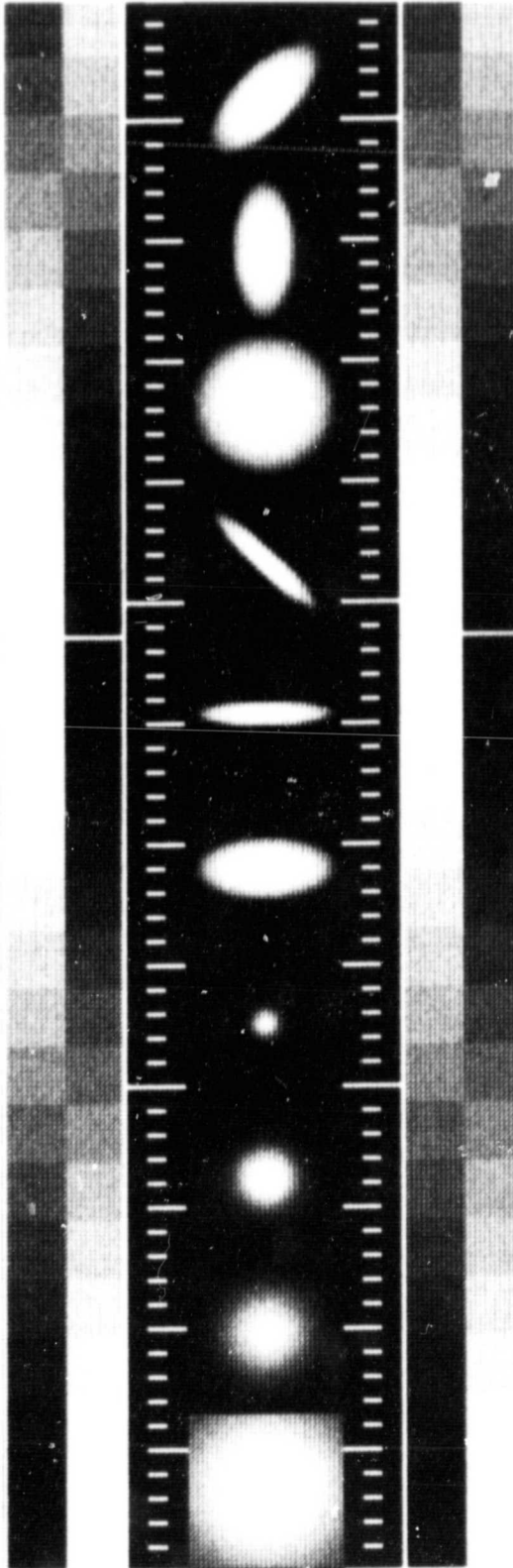
For the purposes of this test, the CLOUDCLS program was modified to measure the attributes of the simulated FFT rather than of the 'clouds.' For example, 90 degrees was subtracted from the direction parameter since the axis of elongation of the FFTs is perpendicular to that of the clouds. This action permitted easier visual assessment of CLOUDCLS computations of the test data. Changes in software should not have any significant effect on computational accuracies.

Results of testing the simulated FFTs (Figure 14) indicate that the direction parameter is in error by no more than 2 degrees, size is reasonably consistent and repeatable, and shape is reasonably consistent and possesses good discrimination. The test data suggest very good potential for measuring physical attributes from FFTs.

#### 4.6 Statistical Attributes

The statistical properties of mean brightness and standard deviation (STD) were calculated for each  $64^2$ ,  $32^2$ , and  $16^2$  box in the original data through the use of a moving spatial (box) filter. The raw data used for calculating mean and STD were not exactly the same as for making the physical attributes, because the moving spatial filter required an odd box size (e.g.,  $31 \times 31$ ) and corner data in the FFT were left out during the process of making the polar coordinate image. The difference in data source areas is considered insignificant. Mean brightness was scaled by a factor of 5, and STD was scaled by a factor of 18 in order to adjust their range of outputs to correspond to the histogram range of the physical attributes.

Mean cloud brightness was selected as an attribute because it relates to the amount and opacity of the cloud. STD was chosen because it is a measure of



|           |     |     |     |     |     |     |     |     |     |     |
|-----------|-----|-----|-----|-----|-----|-----|-----|-----|-----|-----|
|           | 1   | 2   | 3   | 4   | 5   | 6   | 7   | 8   | 9   | 10  |
| SIZEmaj   | 240 | 186 | 137 | 33  | 229 | 197 | 200 | 234 | 223 | 230 |
| SIZEmin   | 240 | 186 | 137 | 33  | 82  | 17  | 19  | 234 | 82  | 97  |
| SHAPE     | 255 | 255 | 255 | 255 | 51  | 6   | 6   | 255 | 51  | 54  |
| DIRECTION | -   | -   | -   | -   | 0   | 0   | 136 | -   | 90  | 46  |

Figure 14. A test of the CLOUDCLS algorithm to generate proper attribute information from simulated FFT images. For ease of viewing, the CLOUDCLS software was modified for this test to measure the attributes of the simulated FFTs rather than of the 'clouds.' All attribute members are scaled through the range 0-255.

statistical texture, or relative change in pattern. Figure 15 shows the six cloud attributes (arranged top to bottom): Mean, STD, Maximum Size, Direction, Shape, and Minimum Size; for the three study dates (across) of 6, 15, and 16 July. The black wedge in the upper right corner masks the California coast, which was excluded from analysis.

#### 4.7 Orthogonality Test

A test of orthogonality was performed on the six channels to insure the relative independence or uniqueness of each. This was done to prevent any duplicate information from biasing the results or unnecessarily diverting attention from more important unique forms of information. The test was a Pearson Correlation analysis from the Statistical Package for the Social Sciences (SPSS). Pixels generated from FFTs over land, and pixels from FFTs considered round by CLOUDCLS were excluded from analysis. The results are shown in Figure 16 and indicate that all six channels approach the complete randomness (relative to each other) that is desired. The highest Pearson 'r' value was .456 for Maximum Size versus Minimum Size, and can be interpreted as meaning that Maximum Size explains  $r^2$  (21%) of the variance in Minimum Size. This poor correlation indicates that the six channels are indeed orthogonal.

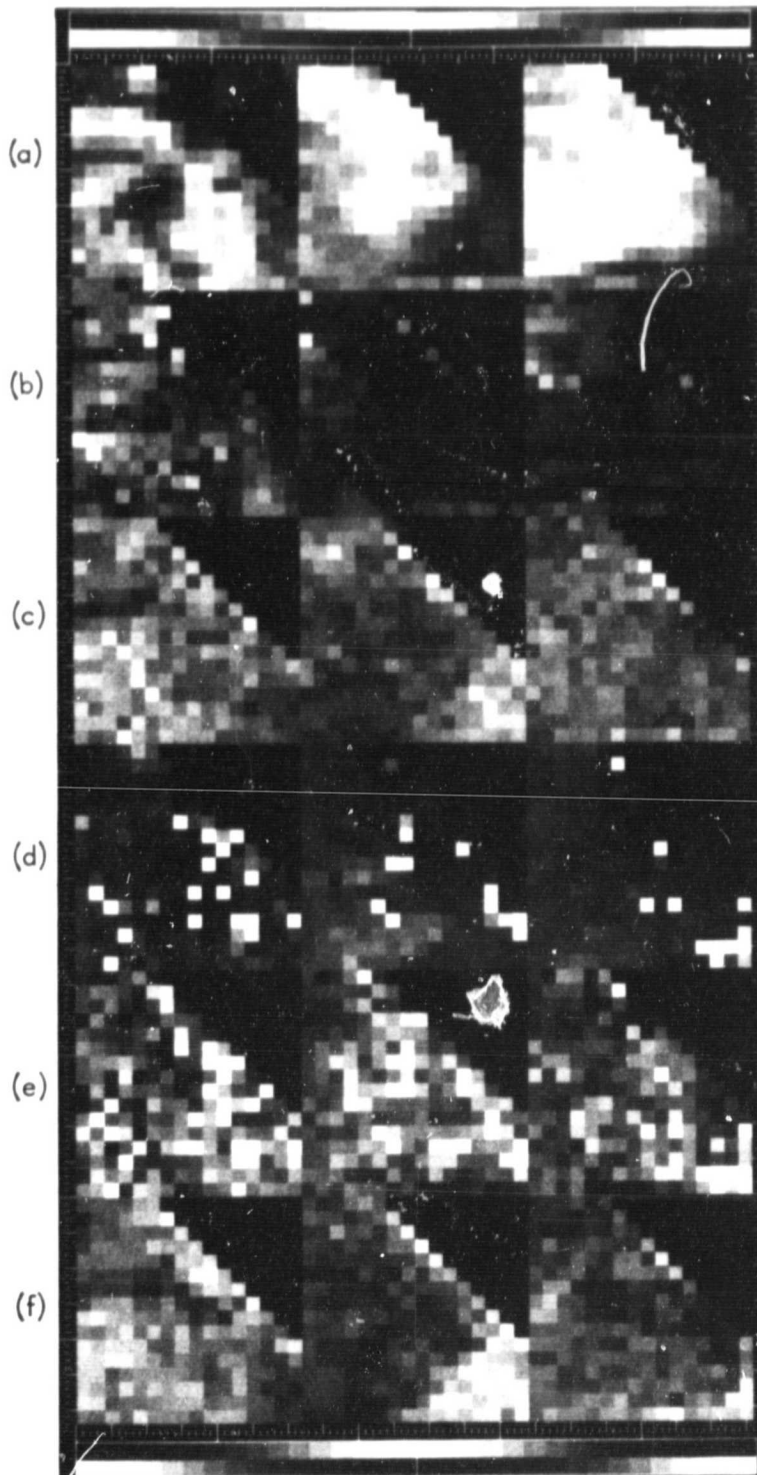


Figure 15. Cloud attribute images produced from FFTs of three GOES visual images: (left to right) 6, 15, and 16 July 1981. From the top are mean brightness (a) and standard deviation (b) produced from statistical calculations. Maximum size (c), direction (d), shape (e), and minimum size (f) were produced from the CLOUDCLS software. Each pixel in the images represents the attribute value extracted from the original 32x32 pixel data. Gray tone range is from black (0) to white (255).

|                                    | MEAN                         | STD                          | MAXS                         | DIR                          | SHAP                         | MINS                         |
|------------------------------------|------------------------------|------------------------------|------------------------------|------------------------------|------------------------------|------------------------------|
| MEAN                               | 1.0000<br>( 191)<br>P=*****  | -0.0755<br>( 191)<br>P=0.150 | 0.1653<br>( 191)<br>P=0.011  | -0.1459<br>( 191)<br>P=0.022 | -0.1219<br>( 191)<br>P=0.046 | -0.2224<br>( 191)<br>P=0.001 |
| STD                                | -0.0755<br>( 191)<br>P=0.150 | 1.0000<br>( 191)<br>P=*****  | 0.0143<br>( 191)<br>P=0.422  | 0.1689<br>( 191)<br>P=0.010  | -0.1929<br>( 191)<br>P=0.004 | 0.1453<br>( 191)<br>P=0.022  |
| MAXS                               | 0.1653<br>( 191)<br>P=0.011  | 0.0143<br>( 191)<br>P=0.422  | 1.0000<br>( 191)<br>P=*****  | -0.0246<br>( 191)<br>P=0.368 | -0.2953<br>( 191)<br>P=0.000 | 0.4560<br>( 191)<br>P=0.000  |
| DIR                                | -0.1459<br>( 191)<br>P=0.022 | 0.1689<br>( 191)<br>P=0.010  | -0.0246<br>( 191)<br>P=0.368 | 1.0000<br>( 191)<br>P=*****  | 0.1708<br>( 191)<br>P=0.009  | 0.3059<br>( 191)<br>P=0.000  |
| SHAP                               | -0.1219<br>( 191)<br>P=0.046 | -0.1929<br>( 191)<br>P=0.004 | -0.2953<br>( 191)<br>P=0.000 | 0.1708<br>( 191)<br>P=0.009  | 1.0000<br>( 191)<br>P=*****  | 0.2407<br>( 191)<br>P=0.000  |
| MINS                               | -0.2224<br>( 191)<br>P=0.001 | 0.1453<br>( 191)<br>P=0.022  | 0.4560<br>( 191)<br>P=0.000  | 0.3059<br>( 191)<br>P=0.000  | 0.2407<br>( 191)<br>P=0.000  | 1.0000<br>( 191)<br>P=*****  |
| (COEFFICIENT/(CASES)/SIGNIFICANCE) |                              |                              |                              |                              |                              |                              |

Figure 16. Pearson correlation matrix of the six cloud attributes. The highest correlation of .456 occurs between maximum and minimum size, and indicates that all channels are basically orthogonal relative to each other.



## 5.0 CLASSIFICATION PROCEDURES

To identify different stratus cloud structure, the six channels of attribute data (Figure 15) were subjected to unsupervised classification. The basic premise of classification is that pixel values of a certain class should be close together in 'measurement space,' whereas data of different classes should be comparatively well separated. The 'unsupervised' component of classification is used when no a priori information is known as to what feature types or classes are present in the data.

### 5.1 Unsupervised Clustering

The first step in unsupervised classification is to cluster the data. Clustering is the process of identifying groups of statistical similarity, and operates in multi-dimensional space, with each overlaid channel (e.g., attribute) representing one dimension. No pixels are assigned to any group; clustering is the process that defines what groups are statistically present based on a user-supplied parameter. Within JPL's VICAR image processing system, unsupervised clustering is performed by the 'USTATS' program. The key parameter is called 'INITIAL,' and defines the maximum statistical difference a pixel can have and still be part of a cluster group. The USTATS software is unique relative to most conventional clustering software in that it does not require the analyst to specify the number of desired clusters. USTATS will continue clustering until it finds all groups exceeding the INITIAL specification or until some external system constraint is reached.

### 5.2 Parallelepiped Maximum Likelihood Classification

VICAR program 'FASTCLAS' (Addington, 1975) brings together the six-channel cloud attribute data set and the cluster groups found by unsupervised clustering to perform the parallelepiped maximum likelihood classification. Classification is the process of assigning a multi-dimensional pixel (i.e., six attribute pixels) to a unique group or class. The FASTCLAS program requires the analyst to specify the 'SIGMA' parameter which sets the limits of a given pixel in multi-dimensional space that cannot be exceeded if it is to be classified. The same SIGMA parameter was applied to each cloud attribute channel although individual channel specifications of SIGMA are possible. SIGMA conceptually specifies the size of the statistical 'window' that a pixel must fall through to be classified. With the FASTCLAS software, a given pixel can experience one of three fates. It may (1) fall through all the statistical windows of one cluster group, permitting it to be classified as a member of that group; it may (2) fall through all the statistical windows of two or more cluster groups, requiring activation of a Bayesian decision rule to decide which cluster it is statistically closer to; or (3) it may not fall through one or more of the windows of a cluster group, in which case it is assigned to the unclassified group. Selection of the SIGMA parameter value is usually performed empirically over several iterations to allow the analyst to interact and 'tune' the classification procedure. Empirical testing for this research suggested a value of 42.5 for the INITIAL parameter and 5 for the SIGMA parameter.

The product of the unsupervised classification procedure is an image with each pixel uniquely assigned to a cluster group. Labeling of the cluster groups is an analyst-intensive operation performed with as much collateral assistance as possible. In this research, the labeling process identifies the linkages between the derived cloud attributes and the cloud structure interpretable from GOES data. The labeling process provides the basis for evaluation of the FFT procedure.

### 5.3 Dendrogram

A measure of statistical separation and similarity between cluster groups can be obtained from dendrogram analysis, which calculates the standardized distance matrix between clusters and uses it to produce a complete linkage diagram (tree). The dendrogram process conceptually 'clusters the clusters' to identify group patterns existing among clusters (Figure 22). The procedure is used to reduce the often overwhelming number of cluster classes to a smaller number that can be evaluated by the analyst.

## 6.0 METEOROLOGICAL ELEMENTS

### 6.1 Collateral Meteorological Information

To identify extant meteorological factors operating in July 1981, a number of sources were queried. The only measurements available for the dates and places under study were collected at Pt. Mugu and San Nicolas Island by U.S. Navy personnel. Surface weather observations and rawinsonde data corresponding to each day of GOES imagery were made available. The majority of these data were not used since the stratus cloud that develops is typically confined to within 1000 feet (303 m) of the surface. Thus, the bulk of rawinsonde observations were not needed (measurements in excess of 60,000 feet are made). Additionally, the location of the two rawinsonde sites on the periphery of the study area effectively reduced their representative utility.

Additional data sources included historical studies on the formation and persistence of the stratus layer (Simon, 1977; Gurka, 1978; Pilie, et al., 1979) and Daily Weather Maps published by the U.S. Department of Commerce. Sea-surface temperature data for selected dates within July were supplied by NEPRF (Section 2.2). The primary problem with these data/information sources is that they rarely matched our needs in either time or space. Accordingly, the bulk of the final analysis had to depend upon photo interpretation techniques.

### 6.2 Meteorological Setting

The formation of stratus clouds off the west coast of central and northern California occurs regularly during summer. Their formation, persistence, and specific variations are dominated by several meteorological controls. Foremost of these are upper-level subsidence and resultant anticyclonic flow, development of an intense low-level inversion, cool water off-shore (California current), and divergence of the southward-flowing air mass.

Typical wind flow patterns off the coast are from the north-northwest sector. The cool California current is clearly indicated in Figure 17, which shows mean sea surface temperature for a typical July. The influence of the dry northwest-north air flow across cool off-shore water plays a major role in the formation of stratus cloud and fog. The thermal differences between low-lying levels also plays a significant role in the rate at which the stratus cloud dissipates during the day.

Because stratus cloud patterns that develop off-shore are all controlled by the same basic factors, the intensity of any one control (inversion height, wind flow, sea-surface temperature, divergence) or their particular combination determines the specific pattern variation that is seen on the GOES images. The pattern shown on the series of July images (Figure 2) is of the same general type, but with many variations. In one typical case, if air flow is from warmer to colder water off the California coast (Figure 17) and large-scale meteorological divergence remains basically constant, the boundary layer cools, dries, and becomes shallower. With these conditions, the cloud base

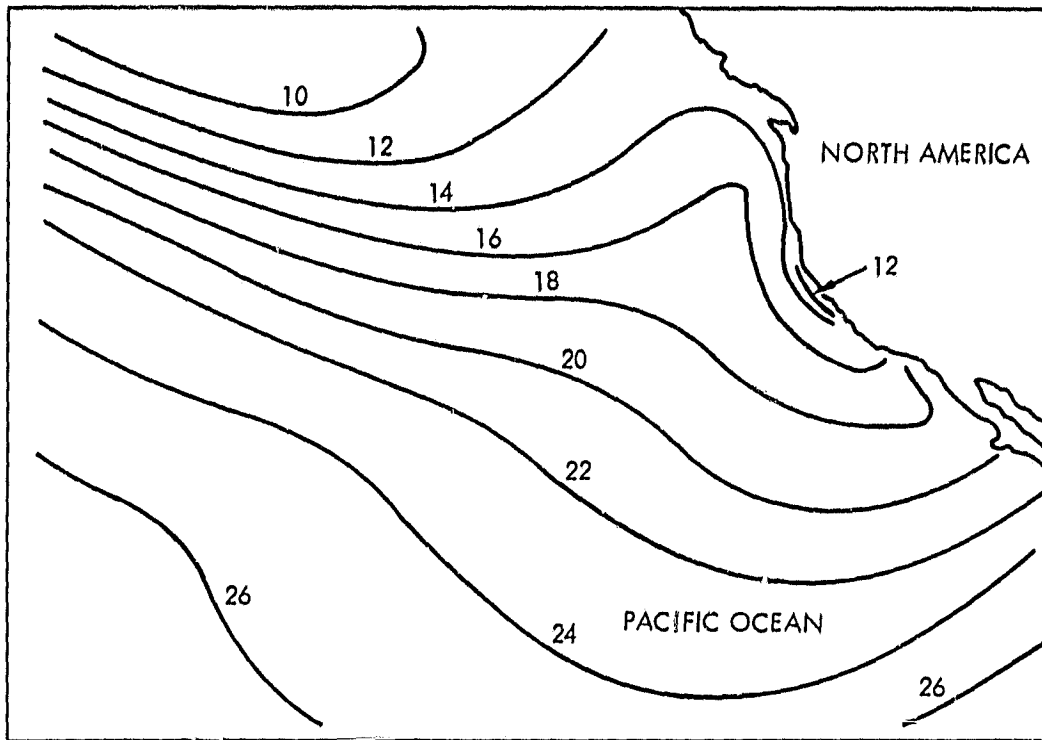


Figure 17. July mean Sea Surface Temperature in degrees Celsius. (Adapted from Schubert, et al., 1979).

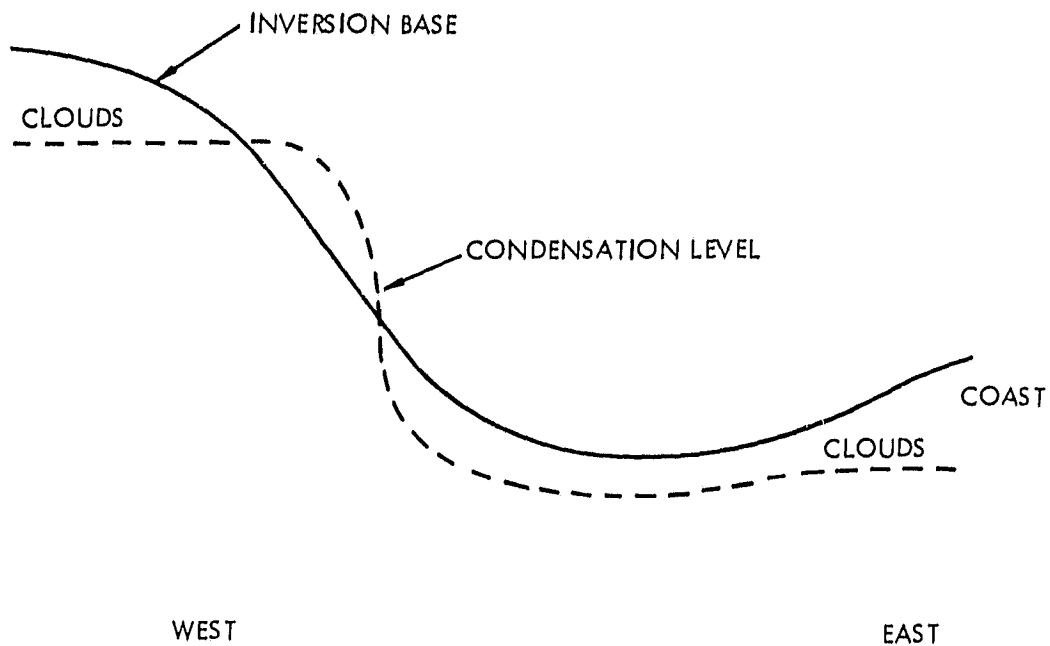


Figure 18. A generalized cross-section of cloud formation from off-shore to the coast. (Adapted from Simon, 1977).

lowers and surface fog can result. Divergence alone can play an important role in determining cloud top height.

A cross-section of cloud formation from off-shore to the coast is diagrammed in Figure 18 (adapted from Simon, 1977). During a typical July, the zero divergence line parallels the California coast off-shore, and inversion lowering plays an important role in determining the variation of stratus or fog pattern that results. Where the inversion is highest (west) cloud types (Figure 18) are higher and divergence is moderate. In the central portion of Figure 18, where the inversion layer drops rapidly, divergence is at a maximum (typically at 125° W longitude). With increasing proximity to the coast, a sea breeze circulation pattern develops due to continental heating, and the typical southerly flow of air is modified. Near the coast, convergence dominates.

West of the line of maximum divergence, divergence is moderate and the inversion layer is highest. The influence of continental heating is negligible here. As the marine air flows south and south-southwest, it passes over warmer water and is heated from below. The resultant cloud pattern can be described as a Benard cell, displaying cellular stratus clouds of variable size and closure.

Another controlling factor in fog/stratus cloud development appears associated with surface geomorphology in the the Pacific Ocean Basin. An often recurring pattern of dense fog/stratus formation aligns perpendicular to the California coastline paralleling the Murray Fracture Zone north of Pt. Conception. As the southward flowing cold California current encounters the subsurface feature, additional upwelling of cold water can occur and may result in enhanced fog formation, as visible in the GOES image of 16 July 1981 (Figure 2).

Pockets of warm water can also lead to specific low stratus formation and/or fog patches. The mechanisms by which this can occur are discussed throughout the literature, but are explained well by Pillie, et al. (1979). Surface observations from San Nicolas Island, GOES data, and sea surface temperature data from 16 July 1981, indicate that several warm water pockets seen on the sea surface temperature image (Figure 3) correlate well with surface observations and visual interpretation of the GOES image (Figure 2) for fog/stratus formation.

Figure 19 indicates the dominant controls and synoptic conditions that exist during periods of off-shore stratus development. The primary elements are upper-level subsidence out of the subtropical high pressure cell and the formation of an intense low-level temperature inversion, the base of which generally lies near or below 1000 feet. The anticyclonic flow from the upper level subsidence results in a generally N to NW light wind throughout the area. Only when the shore is approached does the thermal contrast between land and sea direct air flow to the east as an onshore breeze.

Surface observations indicated haze and scattered clouds at Pt. Mugu (on the mainland) and off of San Nicolas Island. Lowering of the inversion base from San Nicolas Island to Pt. Mugu (west to east) is characteristic of the

ORIGINAL PAGE IS  
OF POOR QUALITY

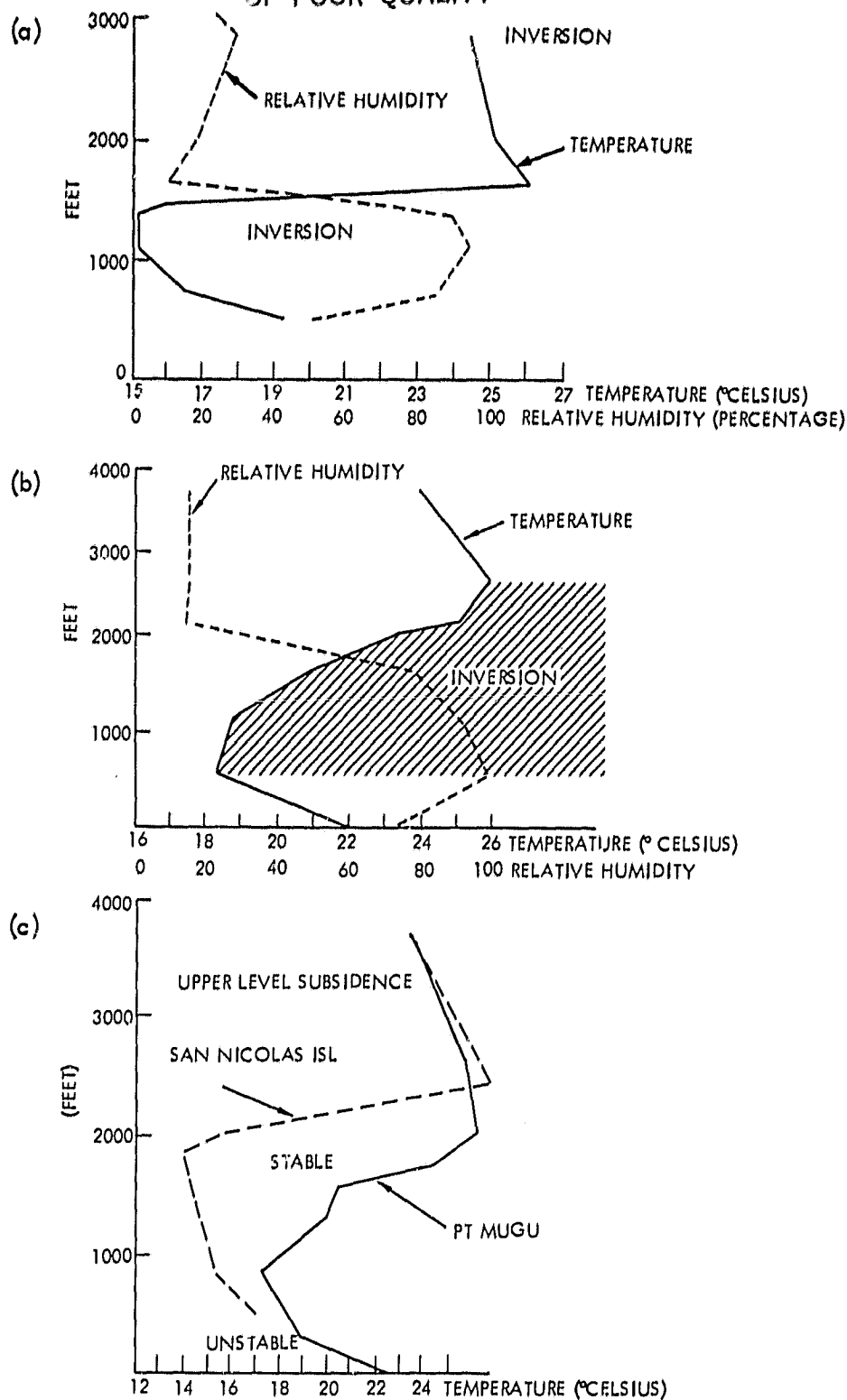


Figure 19. Rawinsonde data of 16 July (a) from San Nicolas Island at 2151 GMT (Greenwich Mean Time), 2246 GMT (b), and combined 17 July data from San Nicolas at 1625 GMT and from Pt. Mugu at 2250 GMT (c).

ORIGINAL PAGE 19  
OF POOR QUALITY

inversion layer during summer. The greater intensity of the inversion off-shore is also clearly illustrated in Figure 19, which plots the 16 and 17 July 1981 rawinsonde data for both Pt. Mugu and San Nicolas Island. There is a definite similarity between the three graphs in Figure 19, especially with respect to the intensity of the inversion. The change in inversion height and intensity during a typical day is indicated on Figure 20, which plots rawinsonde data from Pt. Mugu for three different hours on 17 July 1981. The expected general lowering of the inversion base during the day is clearly evident.

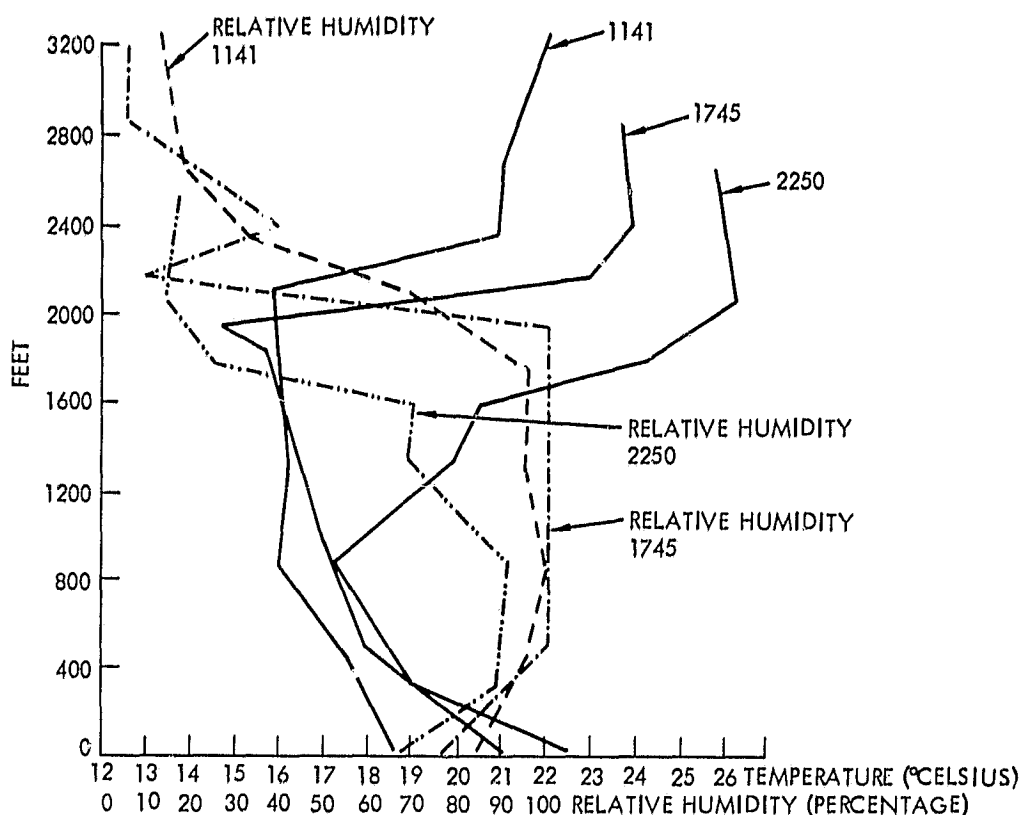


Figure 20. Rawinsonde data of 17 July 1981 from Pt. Mugu showing  
1) the lowering of inversion during the day; and 2)  
that winds are WSW to NW at all significant levels.

## 7.0 CLOUD CLASSIFICATION AND ANALYSIS

Computer classification of three GOES images (6, 15, 16 July 1981) was evaluated to assess the potential for automatic classification of stratus clouds. The purpose of the assessment was to test the accuracy of the classifier to identify type and structure and to determine its ability to repeat the identification on different images. Additionally, the effects of varying the FFT box size were evaluated along with the utility of applying an edge enhancement algorithm prior to FFT generation (Section 8).

Classification emphasis was directed towards discrimination of stratus cloud structure because the GOES data set contained very few non-stratus clouds. The limited nature of the GOES data set and the lack of supporting collateral meteorological information also hindered efforts to relate geophysical parameters to discriminated structural classes. This permitted only a qualitative assessment of the scene independent integrity of the methodology.

### 7.1 32 x 32 Classification

The 32 x 32 pixel box size was selected for intensive analysis because of its minimal data adjustment by apodizing, ease of photo interpretation, and its intermediate position between  $16^2$  and  $64^2$  boxes, which facilitated extrapolation of analysis to those scales. The 16 July 1981 GOES data were selected as the subject of primary analysis because of the range of stratus cloud variation present within the image.

The six cloud attribute images (Figure 15) were evaluated individually and collectively to assess their relative contribution to the classification process. The standard deviation (STD) statistical attribute, which provides a measure of local cloud variation or texture, was found to dominate over the physical attributes of size, shape, and direction. It was dropped from further analysis in order to better evaluate the physical attributes, but should not be discounted from future uses as it provides an independent source of information which may be useful depending upon specific user requirements. The direction attribute was found to be very consistent and reliable except for round clouds, which are indeterminable, and cause a saturation of affected boxes. Shape was determined to be somewhat noisy, but still capable of providing independent and useful information. The use of both size attributes was theorized to provide an overemphasis.

The five attributes were collectively tested in three classifications of the 16 July data by varying the presence of the attribute channels in a stepwise manner. The purpose of the test was to determine which input attributes would provide the best all-around classification with respect to photo interpretation and the limited meteorological data available. Three stepwise classifications were evaluated: 1) Mean, Maximum Size, Direction, Shape, and Minimum Size; 2) Mean, Maximum Size, Direction, and Shape; and 3) Mean, Direction, and Shape. The classifications (Figure 21) were not 'tuned' for maximum information expression; rather, they were standardized for comparison purposes. Each classification was aggregated to present the nine most distinctive classes as defined by dendrogram analysis.



Evaluation of the three classifications indicated that the five-parameter test (Figure 21a) tended to cause a bias in favor of the two size attributes, and that the two used together precluded classification of cloud structure in sufficient detail. Conversely, the three-attribute classification did not provide sufficient discrimination of cloud structure, particularly in the upper left portion of Figure 21c. Excessive aggregation occurred with only the three cloud parameters.

The four-attribute classification (Figure 21b) provided the best discrimination of the cloud type and structure present in the 16 July imagery. A detailed analysis of the raw four-attribute classification was therefore performed using the tree linkage dendrogram and photo interpretation techniques. Figure 22 shows the raw classification with optimally selected class aggregations and dendrogram. Figure 23 displays the resultant ten cloud structural classes overlayed on the 16 July GOES imagery. Legend, grouped classes, key contributing attributes, and structural characteristics that were photo-interpreted from the classes follow:

| <u>Class</u> | <u>Groups</u> | <u>Key Attributes</u> | <u>Label/Characteristics</u>   |
|--------------|---------------|-----------------------|--|
| Lt. Orange   | 10            | Shape, Dir            | Elongated cloud pattern; strong NW-SE directional orientations.  |
| Yellow       | 5,13,19       | Mean, Dir             | Small, rounded, densely packed clouds; dark; NW-SE direction.  |
| Purple       | 6,9,15,17     | Mean                  | Tapering cloud/no-cloud transition; dark small, non-directional cellular clouds.                             |
| Magenta      | 16,18,20      | Mean, Shape           | Wispy, dense, elongated clouds; strong SW-NE direction.  |
| Peach        | 7,14          | Mean, Dir, Shape      | Very densely packed clouds; strong NW-SE direction, formation likely due to onshore flow near coastline.     |
| Dk. Blue     | 1,2,4,12      | Mean, Dir             | Large, rounded cellular clouds; generally non-directional.   |
| Dk. Orange   | 11            | Shape, Size           | Large elongated shapes with mixed and horizontal direction.  |
| Green        | 3             | Mean, Size            | Very small elongated clouds with open patches.   |
| Cyan         | 0,8           | Dir, Shape            | Two classes combined for visual display purposes: 1) excluded areas or indiscriminable clouds; 2) no clouds. |

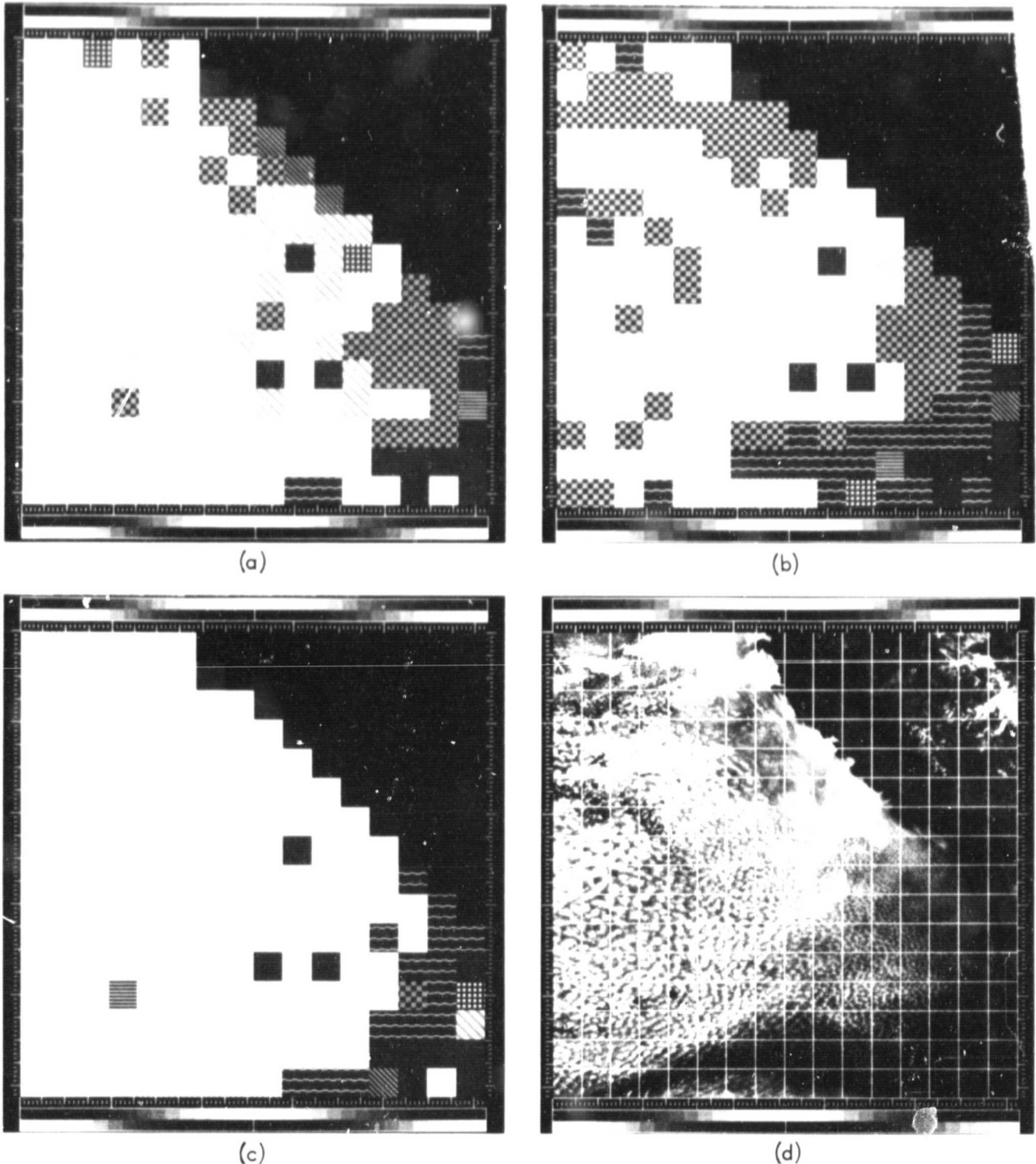
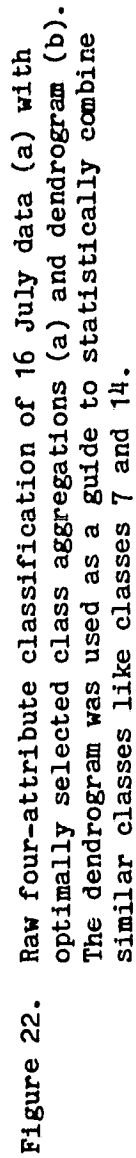


Figure 21. Stepwise cloud structure classification used to identify the best cloud attribute channels. (a) Five-channel classification included mean, maximum size, direction, shape, and minimum size; (b) four-channel classification excluded minimum size; (c) and three-channel classification excluded both minimum and maximum size. The four-channel classification (b) provided the best discrimination of cloud structure. Data are for 32x32 FFTs from 16 July 1981. Classifications were not 'tuned' for maximum information expression, but standardized to show their nine most distinctive classes for comparison purposes.



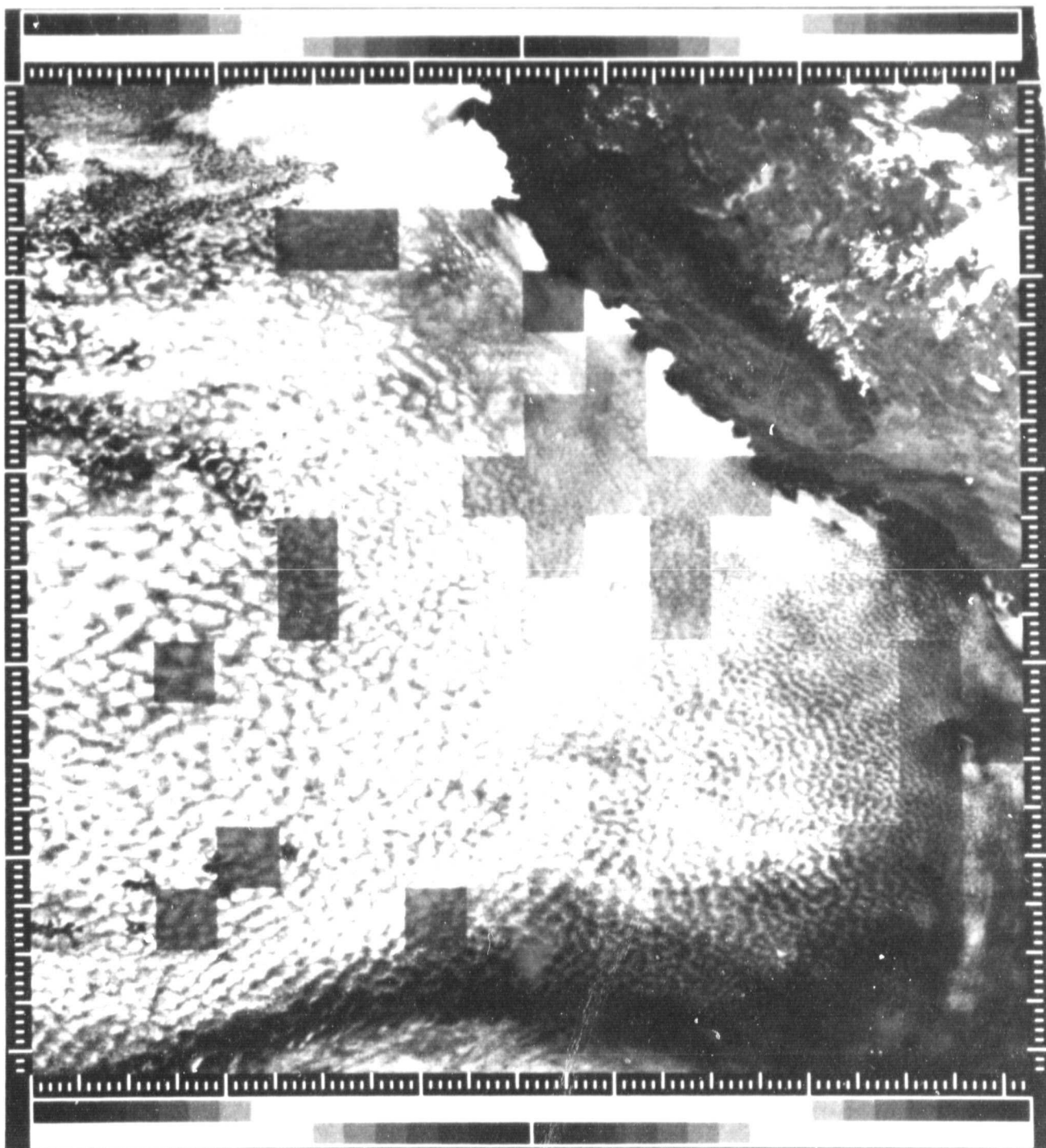


Figure 23. Final 32x32-scale four-attribute cloud structure classification of 16 July 1981 GOES visual imagery. At this 32x32 scale, the classification technique is successfully differentiating cloud structure and pattern based on cloud shape, maximum size, direction, and mean brightness. Legend for color tones can be found in Section 7.1.

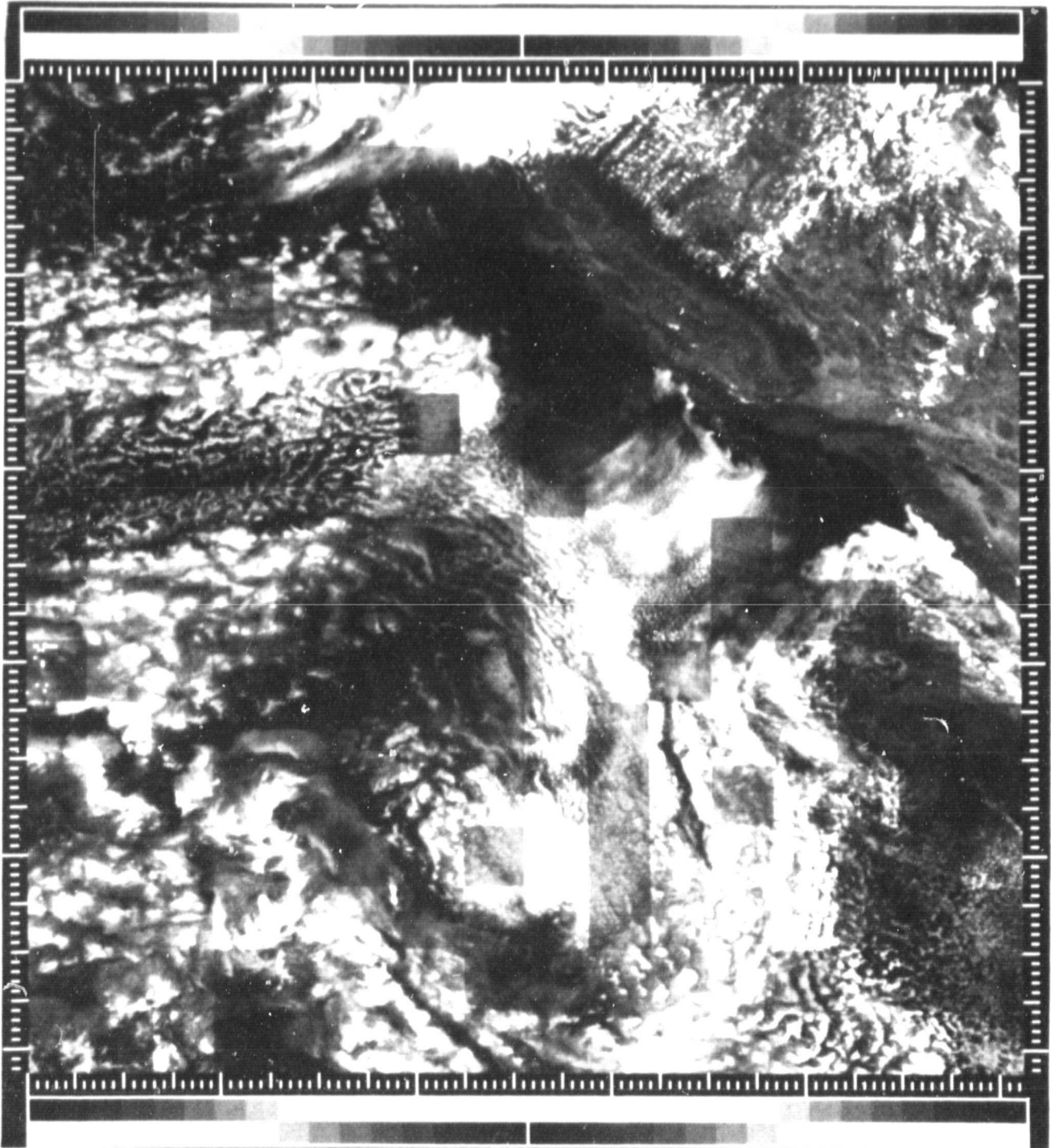


Figure 24. Final four-attribute cloud classification of 6 July imagery demonstrating the scene-independent properties of developed procedures. July 6 image was directly classified using the same cluster statistics and dendrogram groupings from 16 July data. Legend is the same as for Figure 23, and is located in Section 7.1. Cloud structures present in 6 July data but not present in 16 July data were assigned to the 'indeterminant' class (Cyan color).

At the 32x32 FFT size, the classification technique is successfully differentiating cloud pattern based on shape, size, and direction. Although many of the groups noted above have the same characteristic(s), they were not grouped together because of some significant difference in one or more of the attributes. This is especially evident with the direction attribute. For example, classes 10 and 16 (Figure 22) are very similar in terms of shape and size, but markedly different in direction. Class 10 has a very NW-SE trend whereas Class 16 is very definitely NE-SW.

Analysis of the two size attributes in Figure 15 suggests that Minimum size would be superior in operation to Maximum size. Time did not permit retesting the classification substituting Minimum size for Maximum size, but an improvement in the classification could be expected from such an action.

With detailed meteorological data, a more refined evaluation of the ten identified structural classes could be made. From the limited Point Mugu and San Nicolas Island rawinsonde data, it is clear that on 16 July, subsidence and surface cooling caused an inversion at approximately 1500 feet, where it persisted. Below the inversion, winds were from WNW to N, which is implied by the elongated clouds evident in the imagery.

## 7.2 Scene Independence

The 32x32 classification designed for the 16 July image was tested on the 6 July image to evaluate scene independence and reliability of the classification. The 6 July image (Figure 2a), contains a large variety of cloud types, structure, and meteorological processes, especially indicated by the elongated clouds trending northeastward from the crest of the Sierra Nevada. This presented a very different meteorological situation than that occurring on 16 July.

The 6 July imagery was directly classified using the unsupervised cluster statistics derived from the 16 July data (Figure 24). Raw classes were grouped as before, so that legend characteristics derived for the one date were applicable to both classifications. As might be expected, not all of the 16 July classes were present in the 6 July classification, and vice versa. For example, the 6 July classification is missing the Light Orange class, and new cloud structures were assigned to the Cyan-colored 'indeterminacy' class.

Comparison of the two classifications (Figures 23 and 24) indicates a strong degree of scene independence. The large round cellular clouds assigned to the Dark Blue class are reasonably well identified on the image, but perhaps with a slightly stronger directional preference. The transitional cloud/no-cloud non-directional Purple class is also well classified. Perhaps the best indicator of scene independence can be found by comparing the Yellow and Peach colored classes. Both of these classes contain densely packed clouds with a strong NW-SE directionality, but a sharp difference in cloud brightness. These traits are all strongly evident in the 6 July classification.

The prospect for scene-independent classification of clouds using FFT attributes is promising, as indicated by the empirical evidence. This situation occurs because FFTs operate in the frequency domain which is less responsive

to the radiometric and brightness distortions that plague conventional imagery. This suggests considerable potential for development of cluster-based signature banks which could be applied across large extents of cloud imagery. The signature bank concept could be combined with the cloud-atlas/data-base technology developed by Huning, et al. (1982) to potentially produce cloud classifications of the globe.

### 7.3 Scale Analysis

Several FFT box sizes were evaluated to determine the effect of scale on cloud classification. FFT mathematics limit pixel box sizes to powers of two, although changes in pixel resolution would allow intermediate sized areas to become subject to FFT analysis. Box sizes of 8x8 or smaller are not possible because of apodizing problems (Section 3). Box sizes of 128x128 and larger were not investigated because they approached the size of the GOES imagery under investigation (512 lines by 512 samples). Thus, scale analysis was performed by investigation of 16x16 and 64x64 FFT box sizes, and comparison with the results of the 32x32 research already discussed.

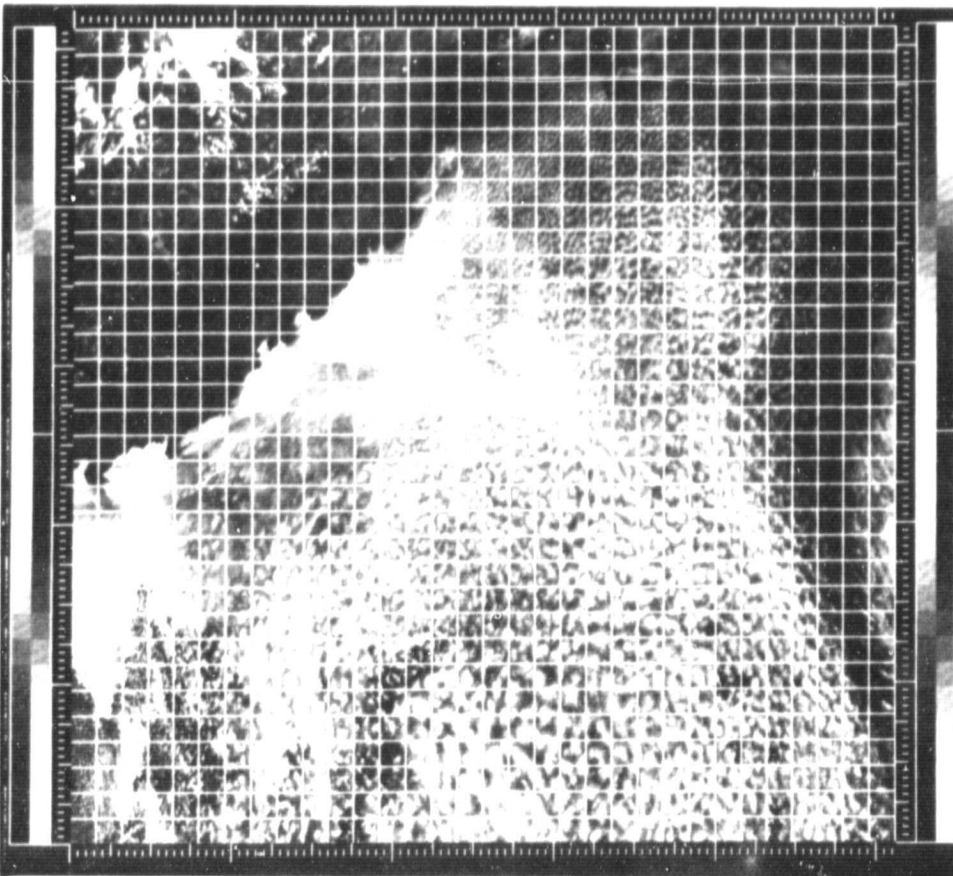
Figure 25a displays the size of the 16x16 grid superimposed on the 16 July image, and the apodized FFTs produced for each box area (Figure 25b). With the scale change from 32x32 to 16x16, a very large number of highly detailed structural classes result from the clustering and classification process. Even with aggregation of similar classes using the dendrogram linkage tree, twenty-four separate classes were identified (Figure 26). The utility of the 16x16 FFTs is that they clearly differentiate cloud structure, but at a sub-geophysical level. The classification appears to be of local cloud parts; few definitive geophysical relationships or trends are evident.

No attempt to describe the twenty-four classes was made except to note specific areas of particular interest. The upper left portion of Figure 25, for example, was differentiated into several distinct classes. Dominance of a particular attribute, whether size, shape, direction, or mean, is evident. The size attribute especially differentiates the large number of circular cloud structures in the imagery. The no-cloud or partially clouded FFTs are also well discriminated. The area with the greatest degree of confusion, and perhaps least overall value, is in the lower right corner where no-cloud areas or partial sky obscuration occurs. Here, a large number of cloud classes were identified as being statistically very separate, but the utility of such fine differentiation is questionable.

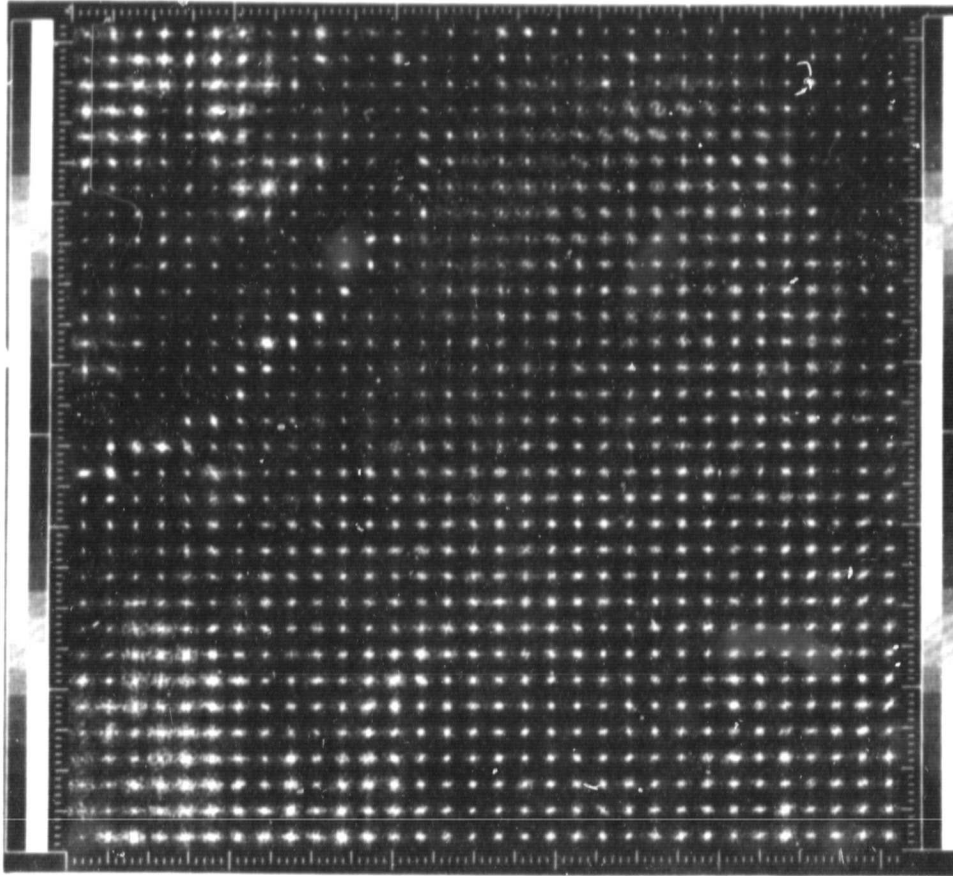
The 64x64 FFT cloud classification was produced using the same procedures and four cloud attributes (Maximum size, Direction, Shape, Mean) used in the 16x16 and 32x32 classifications. As before, the dendrogram was used to group classes, but the large size of the FFTs produced a small number of rather distinctive classes, precluding the need to perform significant class merging.

Figure 27 displays the 64x64 FFTs and resultant classification. Clearly, this classification is identifying cloud type (e.g., stratus type) at the expense of structure. Many of the cellular clouds are grouped together with differentiation occurring primarily with the no-cloud condition, or elongated clouds that have a strong directional preference. The major difficulty with





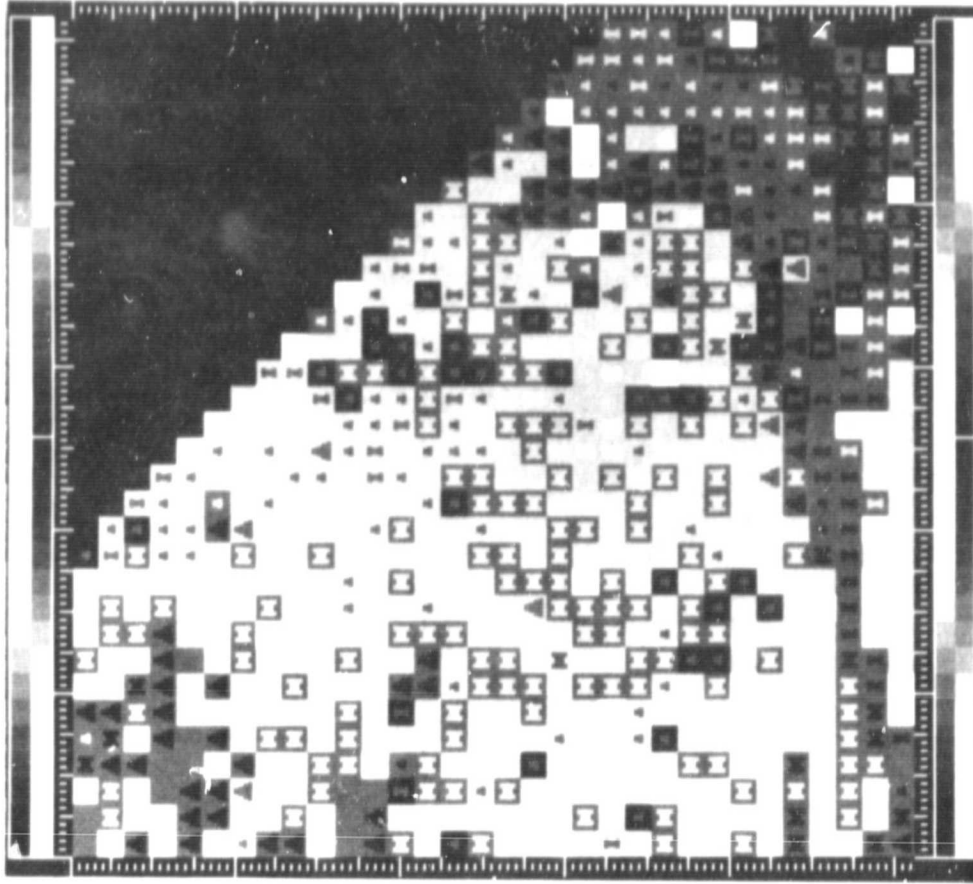
(a)



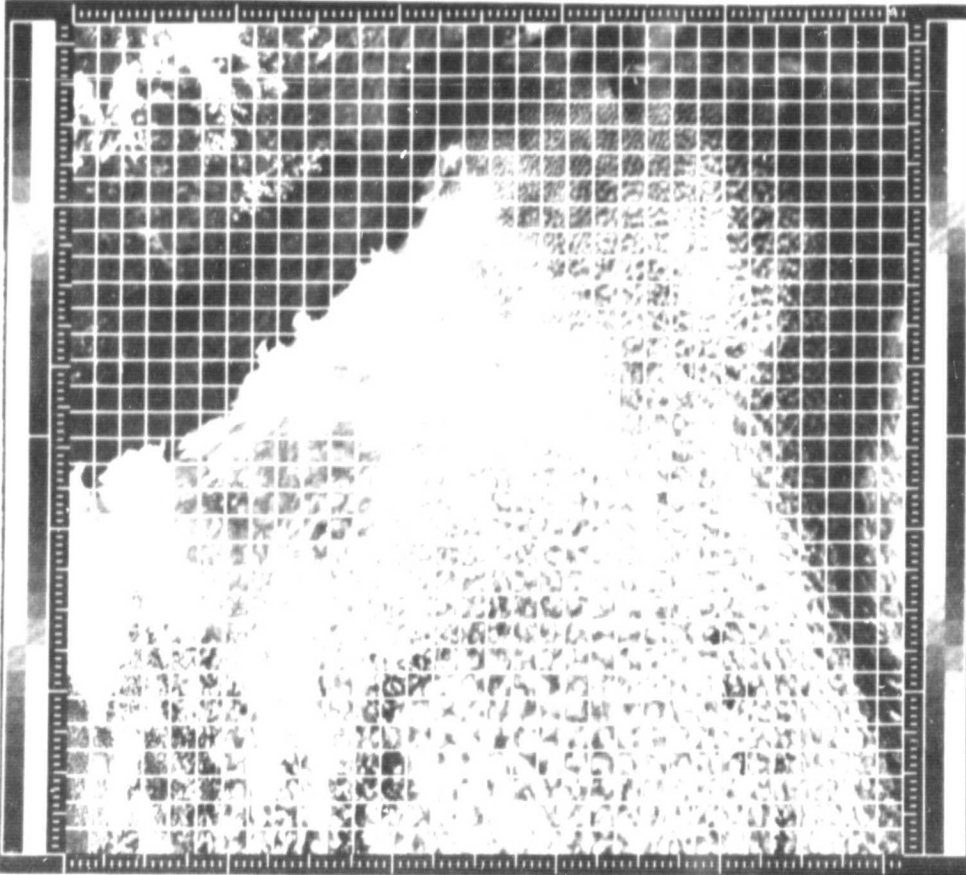
(b)

Figure 25. GOES imagery of 16 July with overlaid 16x16 pixel grid (a) and the apodized FFTs produced from each box (b). FFTs indicate higher level of detail than for 32x32 FFTs (Figure 5).



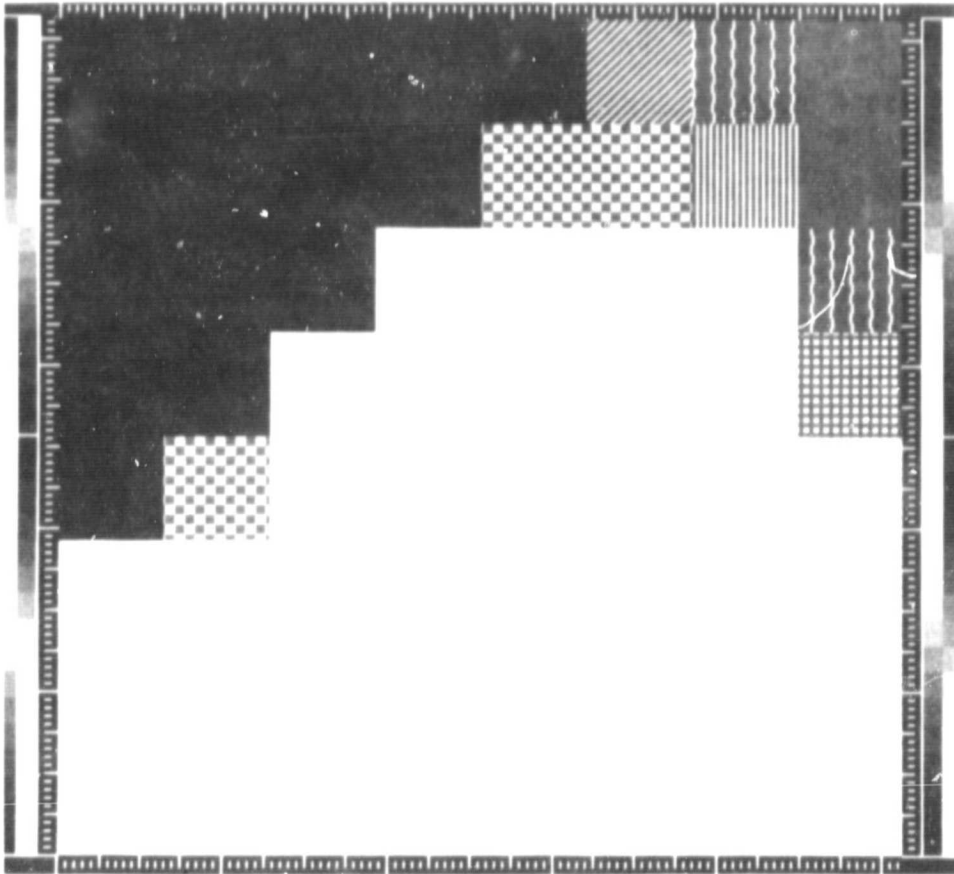


(b)

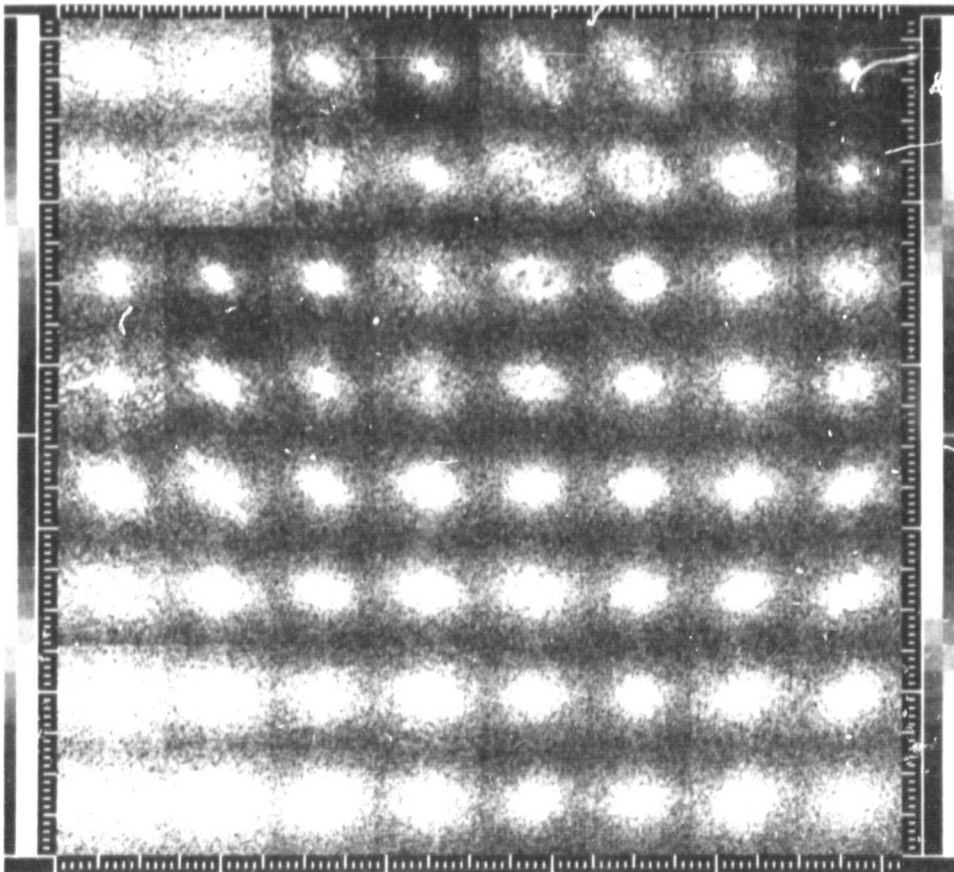


(a)

Figure 26. Final 16x16-scale four-attribute cloud structure classification of 16 July GOES imagery (b) showing twenty-four classes grouped from the original fifty formed. Classification of 16x16 FFTs clearly differentiates cloud structure, but at a sub-geophysical level.



(b)



(a)

Figure 27. Final 64x64-scale four-attribute cloud classification of 16 July  
GOES imagery (b). Classification may be identifying cloud type  
(as opposed to structure), since important structural areas  
appear to be missing. Review of FFTs (a) suggests a consider-  
able reduction in information relative to Figures 5 and 25b.

this classification is the similar grouping of all clouds in the upper left portion of the image where significant variation actually exists. Legend characteristics for the 64x64 classification are:

| <u>Class</u>        |               |   |
|---------------------|---------------|---|
| <u>Designations</u> | <u>Groups</u> | <u>Characteristics</u>  |
| A                   | 7,12          | No cloud or indeterminacy.  |
| B                   | 4,8           | Partially clouded, variable cloud structure.                                  |
| C                   | 6,10          | Small, dark, round-to-elongated clouds.                                       |
| D                   | 1,2,5         | Cellular to slightly elongated; aggregation of several structures.            |
| E                   | 9             | Island-induced standing wave.   |
| F                   | 3             | Wispy, elongated clouds of SW-NE direction; moderate wind suggested.          |
| G                   | 11            | Well-defined elongated clouds; primarily cellular, with NW-SE directionality. |
| H                   | 0             | Land; outside study area.   |

Although the 64x64 classification satisfactorily defines dominant cloud patterns, the large size of the FFT box results in differentiation becoming a function of some very dominant feature such as cloud/no-cloud transition (e.g., Class B), or oddities (e.g., Class F). This situation contrasts most explicitly with the 16x16 classification which appears to provide local cloud structure detached from regional trends. The best classification for defining cloud structure that is relatable to geophysical trends appears to reside with 32x32 FFTs of two-mile GOES imagery.

## 8.0 EDGE ENHANCEMENT ANALYSIS

Fast Fourier Transforms express information that is related to the frequency domain of pattern. An effort was therefore undertaken to enhance the periodicity of cloud edges for the purpose of exposing the underlying cloud pattern often suppressed by low-frequency spatial transitions. A standard deviation (STD) spatial filter was applied to the GOES visual imagery to enhance cloud edges and improve the quality of FFT size, direction, and shape attributes. Unsupervised clustering and classification were performed as with the raw data.

### 8.1 Image Convolution

The standard deviation of a local block of pixels in a satellite image is usually not large because of the blending and overlap common within and between satellite pixels. Thus, to generate STD convolutions of raw GOES imagery, the STD computation must be scaled. From empirical tests, a scaling factor of 18X was determined. The STD for each pixel was computed using a 3x3 pixel moving spatial filter, which calculated the STD for the nine local pixels, added 0.5, and multiplied by 18.0 (Figure 28). The same scale factor was also found to satisfactorily expand the dynamic range of the STD convolved thermal infrared data (Figure 29).

FFTs of the STD imagery were generated using the same techniques as for generating FFTs from the raw GOES imagery. However, it was determined that in using the same technique, much of the FFT data was being saturated at both the high and low end. In section 2.1, it was noted that a scaling factor of 9.7656 was applied to the FFT 'complex' number to introduce compatibility between JPL and NEPRF software. To remove the saturation resulting from the STD convolution, empirical testing determined that '3.5' was a more appropriate scaling factor. Figure 30 compares the two scaling factors for the 16 July visual data.

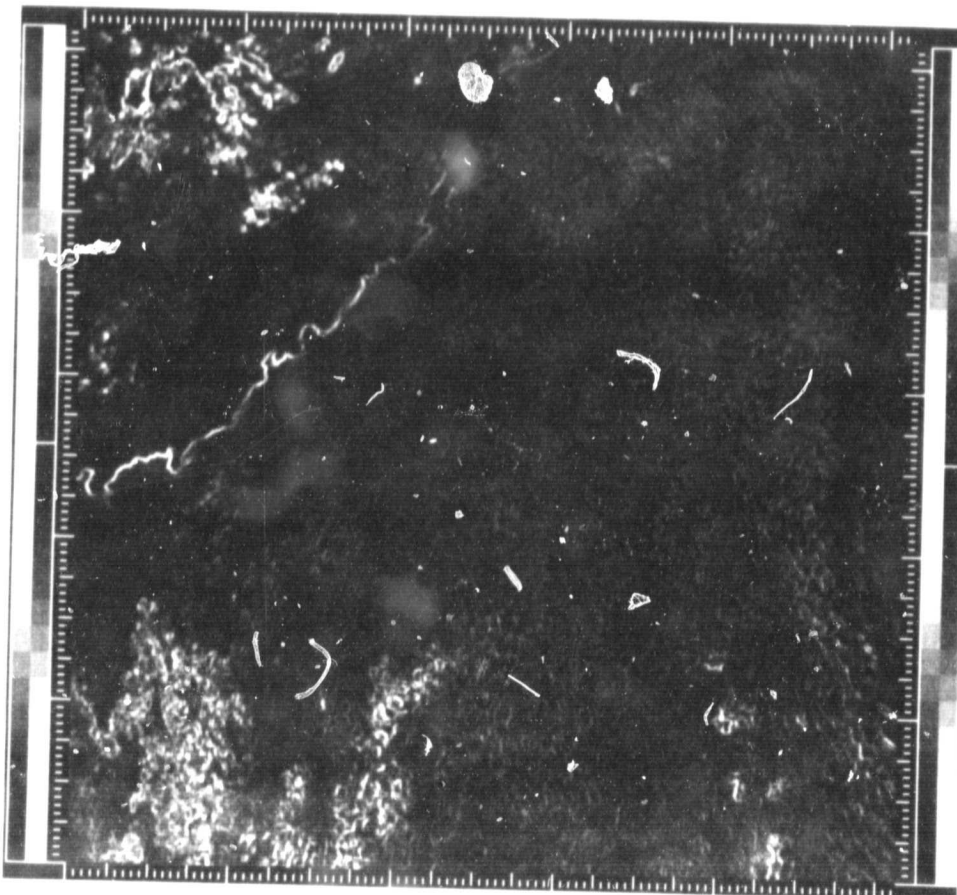
A modification of CLOUDCLS software was necessary for generation of cloud attributes from FFTs of STD convolved imagery. The modification consisted of adjusting the dynamic range of the size attribute's post-stretch. No change in the calculation of the attributes was necessary. The modification to CLOUDCLS was made by adding user-supplied GAIN and OFFSET parameters. The versatility of these parameters extends the use of CLOUDCLS to a variety of types of satellite data (via FFTs).

### 8.2 Classification

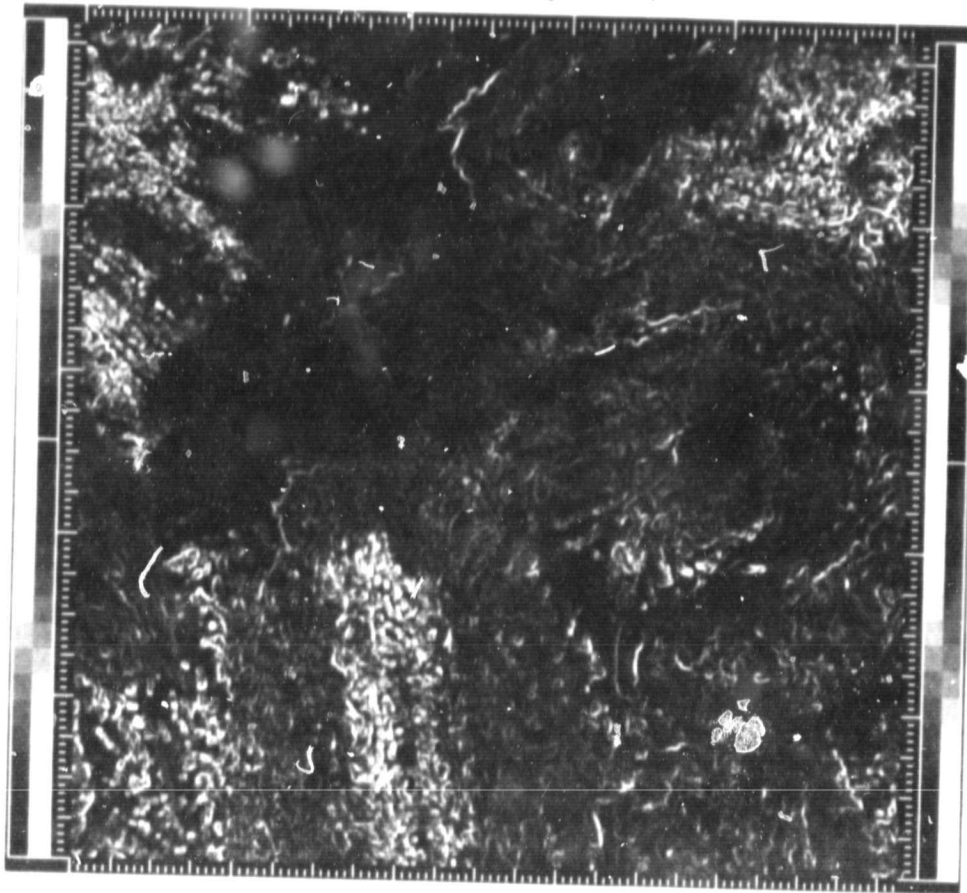
Figure 31 displays the 32x32 cloud attributes derived from STD convolved data for 6, 15, and 16 July. Comparison with the cloud attributes derived from unprocessed GOES imagery (Figure 15) reveals many rather dramatic differences. Qualitative analysis of the attributes suggests that a loss in the discrimination of small clouds occurs relative to those derived from unprocessed data. The reason appears to be that small clouds are 'smeared' by virtue of the finite box size necessary for computing STD images. The 3x3 pixel spatial filter is too large relative to the small size of the clouds to

highlight their cloud/non-cloud boundaries. The likely cause is that too much adjacent cloud is being included in each 3x3 filter calculation. The 'smear' destroys cloud directionality information, and with that loss goes any possibility of computing size or shape. For example, the elongated clouds near the coast in the 16 July imagery were calculated to be round or indeterminate by CLOUDCLS. This problem can essentially be considered a matter of scale. Finer spatial resolution imagery would reduce the problem.

Figure 32 shows a 32x32 classification of the 16 July STD convoluted imagery based on the four physical attributes shown in Figure 24. The small cloud problem is clearly evident in the lower right area near the coast, where the NW-SE diagonal class pattern includes both small clouds and the densely packed clouds farther up the coast. A second problem occurs in the bottom right corner where a greater number of distinct classes are identified by the classifier than are warranted. An interesting feature of the STD classification is the checker-board class in the middle of Figure 32. This feature is largely the product of the size maximum attribute, which is identifying that region as an area of 'small' clouds (smaller than the small clouds in the southeast corner). Proper classification would identify them as medium-sized clouds.

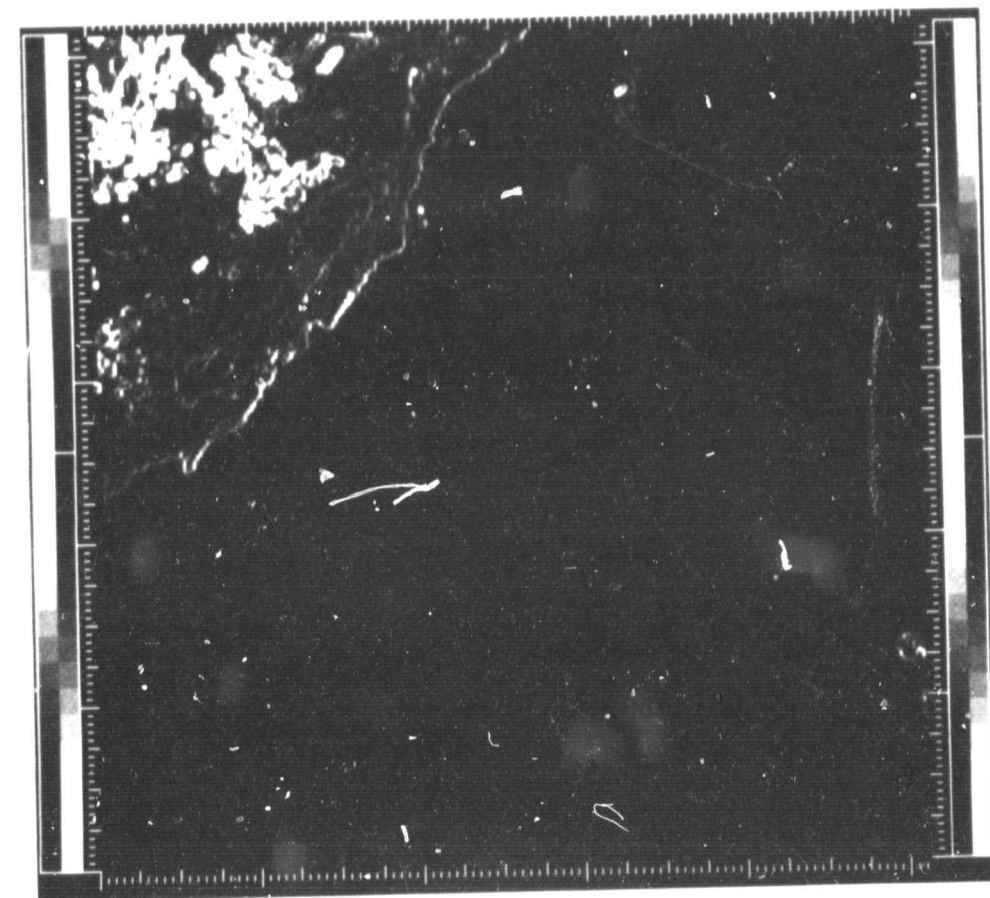


(a)

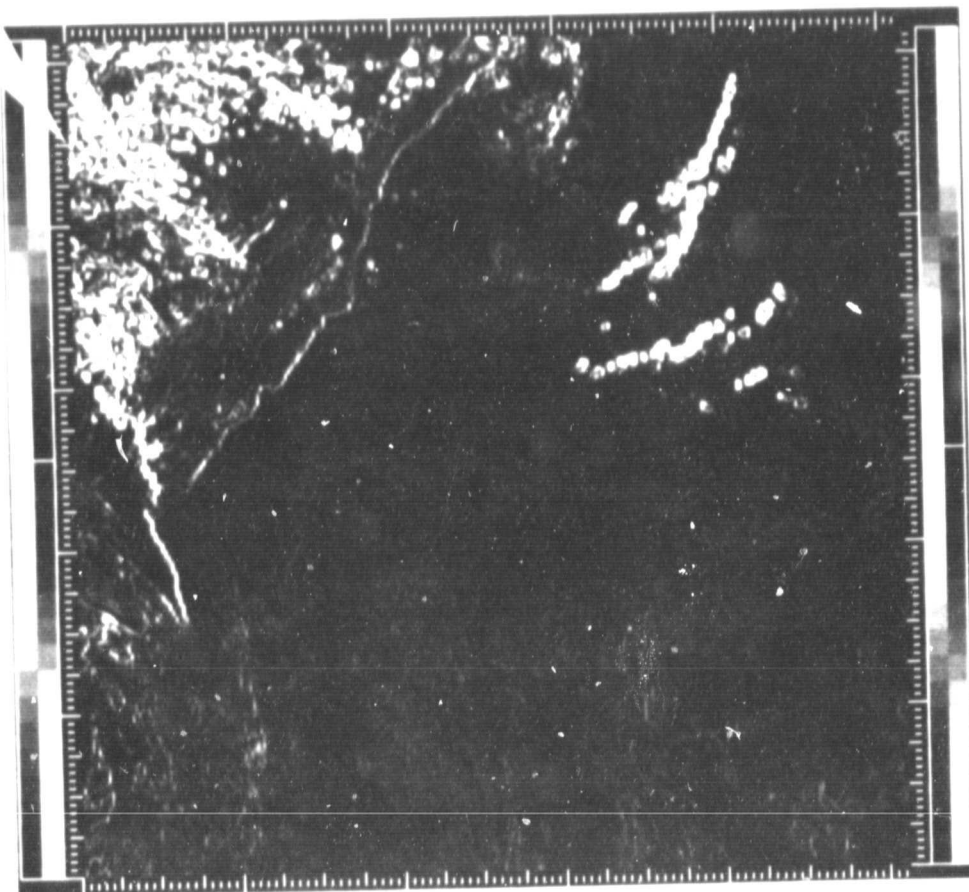


(b)

Figure 28. Standard deviation convolution of 16 July (a) and 6 July (b) GOES visual imagery. Convolution was performed by passing a 3x3 pixel moving spatial filter over data and scaling the result.



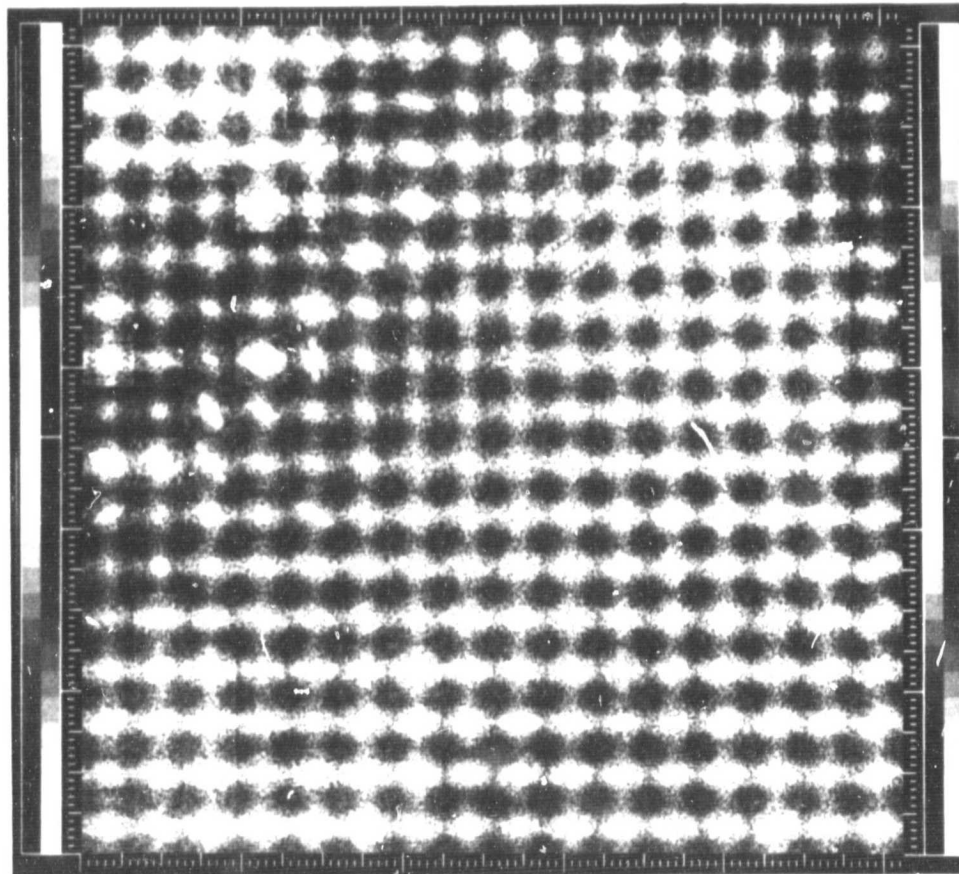
(a)



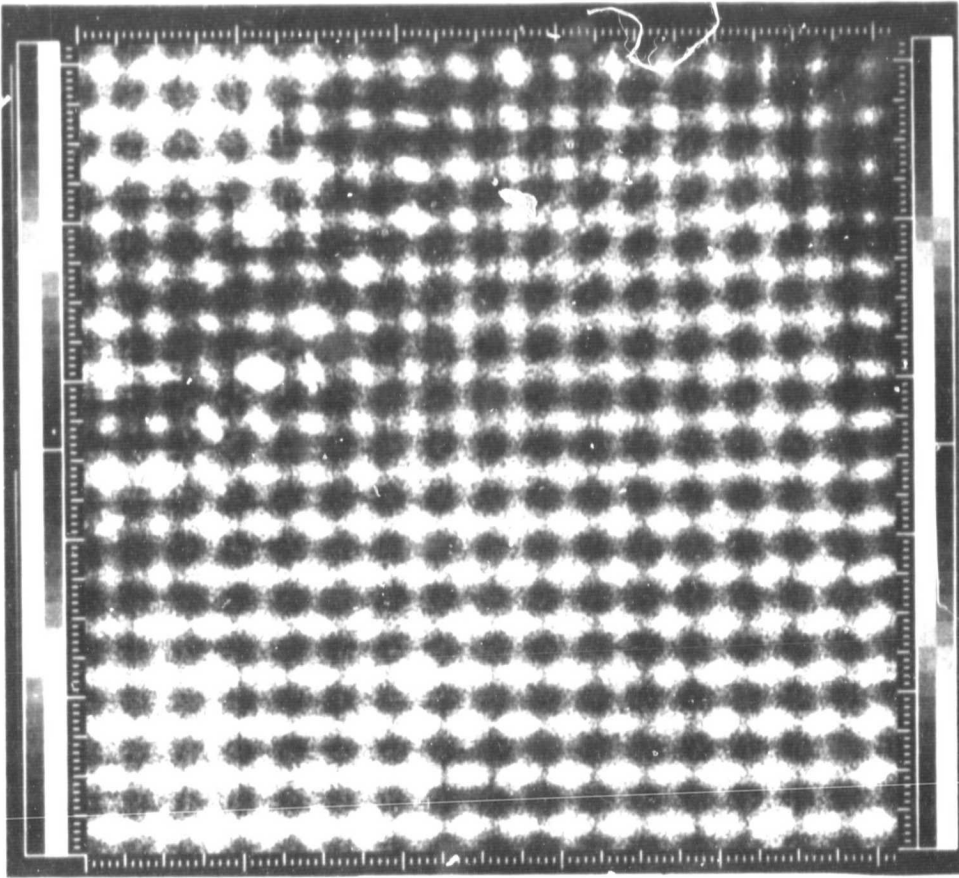
(b)

Figure 29. Standard deviation convolutions of 16 July (a) and 6 July (b) thermal infrared imagery.





(a)



(b)

Figure 30. FFT images of standard deviation convolved GOES visual data. The internal scaling factor of 9.7656 (a) used for raw GOES imagery (Figures 5, 25b, 27a) was changed to 3.5 (b) to reduce saturation.





Figure 31. Cloud attribute images produced from FFTs of three standard deviation (STD) convolved visual GOES images: (left to right) 6, 15, 16 July 1981. From top to bottom are maximum size (a), direction (b), shape (c), and minimum size (d). Comparison with Figure 15c-f reveals major differences resulting from the STD convolution, and the general loss of information associated with very small clouds.

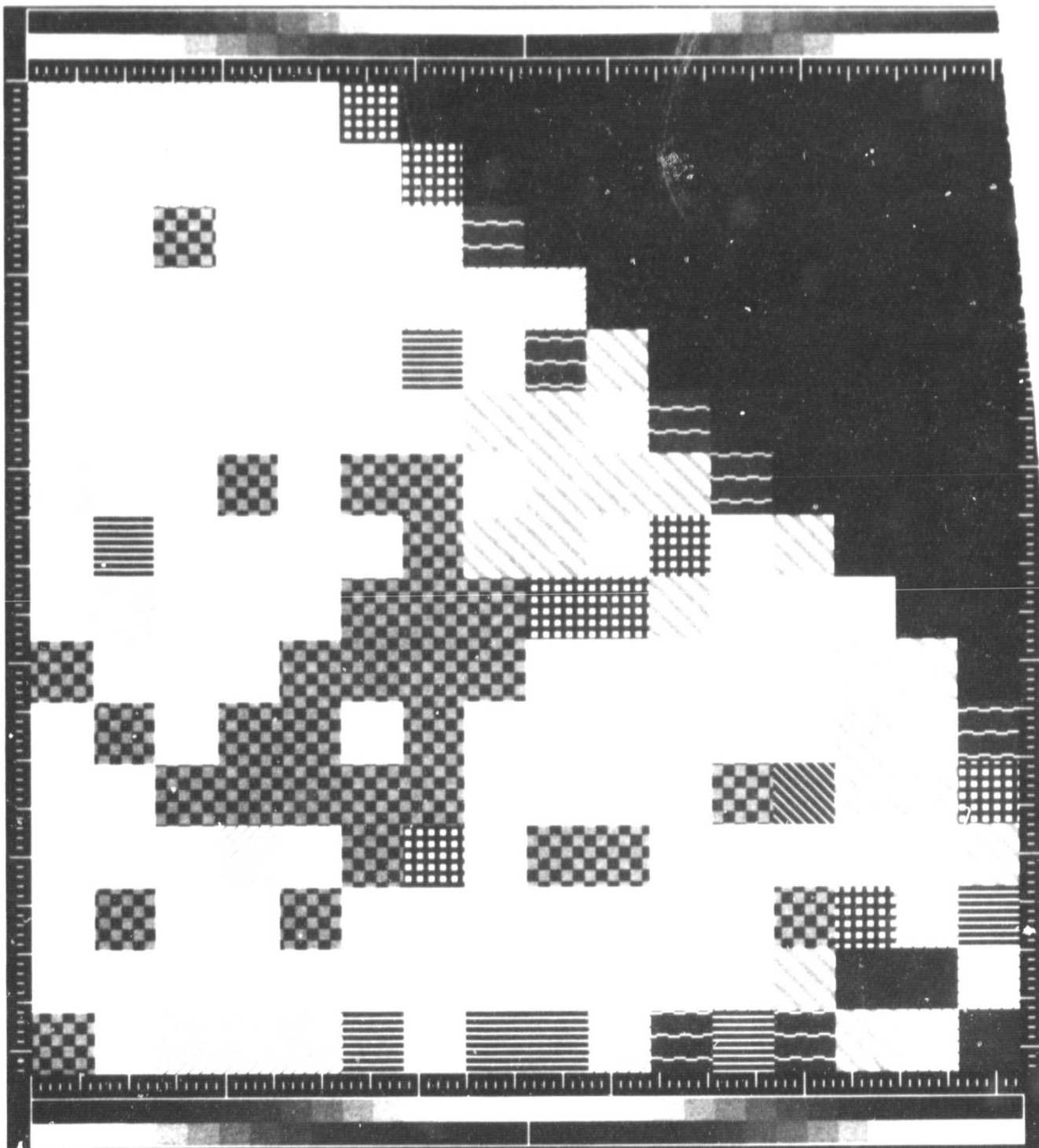


Figure 32. Final 32x32-scale four-attribute classification of standard deviation-based attributes (Figure 31) of 16 July data. Classification used only FFT attributes (maximum size, direction, shape, and minimum size), and they experienced problems with small cloud areas.

## 9.0 CONCLUSIONS AND RECOMMENDATIONS

### 9.1 Conclusions

GOES imagery of the California coast for July 1981 were used to test the feasibility of using 2-D FFTs for automatically typing clouds, and possible identification of dominant meteorological controls. The test case employed imagery displaying variable patterns of what are typically called stratus clouds. The assumption was made that this particular cloud type, because of its characteristically homogeneous occurrence across the test images, would allow reasonable test of the developed classification methodology.

The approach consisted of extracting three cloud attributes (shape, direction, size) and a statistical attribute (mean brightness), from Fast Fourier transforms derived from GOES data, and subjecting them to unsupervised clustering and parallelepiped maximum likelihood classification. The approach appears promising. However, the limited nature of the assembled GOES data set and supporting collateral meteorological information presently permits only a qualitative analysis and assessment.

Specific results indicate that: 1) the key cloud discriminating attributes are mean brightness, direction, shape, and minimum size; 2) cloud structure can be differentiated at the 16x16 and 32x32 scales; 3) cloud type may be identified at the 64x64 and coarser scales; 4) there are positive indications of scene independence which could permit development of a cloud signature bank; 5) edge enhancement of GOES imagery does not appreciably improve cloud classification, although it may do so with the use of finer resolution spectral data; and 6) the GOES imagery must be apodized before generation of FFTs.

### 9.2 Recommendations

To determine (1) if the FFT-based classification approach is scene-independent; (2) if discriminated classes are relatable to geophysical phenomena; and (3) if selected attribute channels are optimal, it is recommended that a new GOES data set with adequate supporting rawinsonde and surface observations be assembled. The GOES data set should consist of at least two accessions of VS and IR data per day taken one-half hour apart. These data should be subjected to NEPRF's cloud tracking software to generate collateral cloud movement vectors, vorticity, and divergence information for each image set. Additionally, for at least one day, half-hour apart accessions should be taken on four to six occasions in order to model the meteorological processes over a full diurnal period. Data should be imaged during July for stratus investigations, and during additional seasons and in other geographic areas for general cloud typing applicability research. Simultaneously, rawinsonde and surface observations should be taken at Pt. Mugu, San Nicolas Island, Monterey, and from ocean vessels if possible. Higher quality sea surface temperature data (perhaps satellite-derived) should be obtained because of its major role in cloud formation.

With sufficient and reliable collateral data, a classification can be interrogated and confidently related to geophysical phenomena. The

ORIGINAL PAGE IS  
OF POOR QUALITY

classification can then be statistically correlated with other classification in a stepwise manner to assist in evaluating the relative importance of each cloud attribute channel. Using a similar correlation procedure, the capability of the classification methodology to produce scene-independent results can be evaluated.

The CLOUDCLS software produces satisfactory cloud attribute information. However, CLOUDCLS software cannot be expected to perform well in areas of excessive cloud variability or where the cloud is bigger than the FFT cell size. A recommendation to reduce this problem would be the investigation of a stratified approach to the classification procedure.

The stratified (or 'layered') classification approach offers potential for automating the entire classification process and improving classification results by removing areas of confusion before classification. For example, the thermal infrared imagery could be processed as the first step in a procedure to identify and label high altitude clouds and land area.

The CLOUDCLS program produces more precise cloud attributes with a 16 x 16 pixel grid cell than with a 32 x 32 grid cell. This is because there is less cloud variation in the cell to degrade the FFT. However, the fine level of structural detail produced by the classification process exceeds the capability of the available meteorological data to explain it. Analysis of the 32 x 32 and 64 x 64 grid cell classifications appears more plausible. It is therefore recommended that future FFT investigations of 2-mile resolution GOES imagery concentrate on 32 x 32 and 64 x 64 pixel grid cells, with the 16 x 16 cells used only if there is a desire for precise local cloud information. This decision, however, is more properly a matter to be decided by the specific user requirements.

## 10.0 REFERENCES

1. Addington, John D., 1975. "A Hybrid Classifier Using the Parallelepiped and Bayesian Techniques," Proceedings of the American Society of Photogrammetry, Washington, D.C. (March) Falls Church, VA., 772-784.
2. Bunting, J.T., and R.F. Fournier, 1980. Tests of Spectral Cloud Classification Using DMSP Fine Mode Satellite Data, Air Force Geophysical Laboratory, Hanscom AFB, Mass. AFGL-TR-80-0181, Env. Res. Paper No. 704.
3. Castleman, K.R., 1979. Digital Image Processing, Prentice-Hall, Inc.: Englewood Cliffs, N. J., 429p.
4. Gurka, J.J., 1978. "The Role of Inward Mixing in the Dissipation of Fog and Stratus," Monthly Weather Review, 106 (September), 1167-1171.
5. Huning, J.R., T.L. Logan, and J.H. Smith, 1982. Cloud Cover Estimation: Use of GOES Imagery in Development of Cloud Cover Data Base for Insolation Assessment, JPL Publication 82-101, Jet Propulsion Laboratory, Pasadena, CA.
6. Pillie, R.J., E.J. Mack, C.W. Rodgers, U. Katz, and W.C. Kocmond, 1979. "The Formation of Marine Fog and the Development of Fog-Stratus Systems Along the California Coast," Journal of Applied Meteorology, 18 (October), 1275-1286.
7. Schubert, W.H., J.S. Wakefield, E.J. Steiner, and S.K. Cox, 1979. "Marine Stratocumulus Convection. Part I: Governing Equations and Horizontally Homogeneous Solutions; and Part II: Horizontally Inhomogeneous Solutions," Journal of Atmospheric Sciences, 36 (July), 1286-1324.
8. Simon, R.L., 1977. "The Summertime Stratus Over the Offshore Waters of California," Monthly Weather Review, 105 (October), 1310-1314.
9. Toldalagi, P.M., and W.M. Lebow, 1982. Survey and Analysis of Satellite Cloud Classification Research Techniques, Naval Environmental Prediction Research Facility, Monterey, CA., NEPRF Contract 81-C-H155. 43p.
10. Twogood, R.E., and M.P. Ekstrom, 1976. "An Extension of Eklundh's Matrix Transposition Algorithm and Its Application in Digital Image Processing," IEEE Transactions on Computing, (Correspondence), (September), 950-952.